ELSEVIER

Contents lists available at ScienceDirect

Optics Communications

journal homepage: www.elsevier.com/locate/optcom





Interference mitigation using optimised angle diversity receiver in LiFi cellular network*

Zhihong Zeng ^a, Chen Chen ^{a,*,1}, Xiping Wu ^{b,c,*,1}, Svetislav Savović ^d, Mohammad Dehghani Soltani ^e, Majid Safari ^{e,*}, Harald Haas ^{f,2}

- ^a School of Microelectronics and Communication Engineering, Chongqing University, Chongqing, 400000, China
- ^b School of Information Science and Engineering, Southeast University, Nanjing 210096, China
- ^c Purple Mountain Laboratories, Nanjing 211111, China
- ^d University of Kragujevac, Faculty of Science, R. Domanovića 12, Kragujevac, Serbia
- e School of Engineering, Institute for Digital Communications, The University of Edinburgh, Edinburgh EH9 3FD, UK
- f Department of Engineering, Electrical Engineering Division, Cambridge University, CB3 0FA Cambridge, UK

ARTICLE INFO

Keywords: LiFi Inter-cell interference Interference mitigation Angle diversity receiver

ABSTRACT

Light-fidelity (LiFi) is an emerging technology for high-speed short-range mobile communications. Inter-cell interference (ICI) is an important issue that limits the system performance in an optical attocell network. Angle diversity receivers (ADRs) have been proposed to mitigate ICI. In this paper, the structure of pyramid receivers (PRs) and truncated pyramid receivers (TPRs) are studied. The coverage problems of PRs and TPRs are defined and investigated, and the lower bound of field of view (FOV) for each PD is given analytically. It is shown that the lower bound of FOV for TPR and PR are 20° and 30°, respectively. The impact of random device orientation and diffuse link signal propagation are taken into consideration. The performances of PRs and TPRs are compared, and optimised ADR structures are proposed by jointly considering the impact of tilt angle, FOV, and the number of PDs. For a transmitter-bandwidth limited system, the optimal PD values are 6 for PR and 9 for TPR, whereas, for a receiver-bandwidth limited system, the optimal PD value is 15. In addition, the double source (DS) cell system, where each LiFi AP consists of two sources transmitting the same information signals but with opposite polarity, is proved to outperform the single source cell (SS) system in interference limited or noise-plus-interference limited scenario. However, the SS cell system outperforms the DS cell system in a noise-limited scenario.

1. Introduction

With the increasing demand for wireless data, the radio frequency (RF) spectrum is becoming a limited resource, prompting the exploration of alternative technologies like Light-Fidelity (LiFi). LiFi is a bi-directional, high-speed wireless communication technology that uses light emitting diodes (LEDs) and photodiodes (PDs) for data transmission through intensity modulation (IM) and direct detection (DD). It offers enhanced security, vast bandwidth, and can be integrated with existing LED lighting to create a LiFi attocell network, which operates alongside wireless networks without RF interference. These advantages make LiFi a promising focus for future research and development [1].

By improving the spatial reuse of the spectrum resources, cellular networks can achieve a higher area spectral efficiency. In comparison with RF femtocell networks, LiFi attocell networks use smaller cell sizes as the light beams from LEDs are intrinsically narrow [2]. Thus, with the densely deployed optical access points (APs), the LiFi attocell network can achieve a better bandwidth reuse and a higher area spectral efficiency. However, similar to other cellular systems, inter-cell interference (ICI) in LiFi attocell networks limits the system performance. This is because the signal transmitted to a user will interfere with other users who are receiving signals from the same frequency resource. Particularly, cell-edge users suffer from severe ICI. Despite the dense deployment of APs, due to ICI, LiFi may not provide a uniform

This work was financially supported by the National Natural Science Foundation of China under Grant 62271091.

^{*} Corresponding authors.

E-mail addresses: zhihong.zeng@cqu.edu.cn (Z. Zeng), c.chen@cqu.edu.cn (C. Chen), xiping.wu@seu.edu.cn (X. Wu), savovic@kg.ac.rs (S. Savović), m.dehghani@ed.ac.uk (M.D. Soltani), majid.safari@ed.ac.uk (M. Safari), huh21@eng.cam.ac.uk (H. Haas).

¹ Senior Member, IEEE.

² Fellow, IEEE.

coverage concerning data rate. Interference coordination mechanisms have been extensively investigated for visible light communication (VLC) systems [3-6]. The commonly used technique is static resource partitioning [7]. By separating any two cells that reuse the same frequency resource with a minimum reuse distance, ICI is effectively mitigated. However, there is a significant loss in spectral efficiency. A combined wavelength division and code division multiple access scheme was proposed in [3]. Although this approach enhances the system bandwidth, it requires separate filters for each colour band and thus creates additional cost. In [4], the fractional frequency reuse (FFR) technique is proposed to mitigate ICI. The FFR scheme is a cost-effective approach to provide improvements both in cell-edge user performance and average spectral efficiency, but a low user-density will decrease the average spectral efficiency significantly. Joint transmission (JT) has been proven to improve signal quality for cell-edge users [5]. The downside of the JT systems is the extra signalling overhead. Moreover, the space division multiple access (SDMA) scheme using angle diversity transmitters proposed in [6] can mitigate ICI by generating concentrated beams to users at different locations.

The angle diversity reception, first proposed in [8], allows the receiver to achieve a wide field of view (FOV) and high optical gain simultaneously. An angle diversity receiver (ADR) is composed of multiple narrow-FOV PDs facing in different directions. In [9-24], the ADR is used to address the issue of ICI as well as frequency reuse in LiFi cellular systems, and different signal combining schemes are investigated. In [12,13], a constrained FOV ADR (CFOV-ADR) is proposed to mitigate ICI. A geometrical model and mathematical analysis for CFOV-ADR are presented in [12], demonstrating that implementing CFOV-ADR can significantly increase the overall capacity of the VLC downlink channel by allowing each transmitter in the network to use the entire optical spectrum. By optimising the photodiode's FOV angle, line-of-sight (LOS) ICI can be completely eliminated, and inter-symbol interference (ISI) can be significantly reduced, with the optimal FOV angle range calculated for a typical indoor scenario [13]. In 2020, an ADR receiver with four branches is considered to enhance the data rate of non-orthogonal multiple access (NOMA) system [14]. The ADR is also utilised for the uplink multi-user (MU) light communication systems in [15,16]. An optimal fair resource allocation (OFRA) scheme is proposed to mitigate both inter-symbol and inter-user interference in uplink multi-user VLC networks. The scheme aims to improve the fairness among the users in terms of their received signal-tointerference-plus-noise-ratios (SINRs) by implementing the ADR [15]. In 2021, the ADR structure is proposed to optimise the uniformity of the received optical power distribution in an VLC system [17]. Simulation results show that the inclination angles and the number of side detectors would affect the variance and average of the received optical power, and the variance would decrease with the increase of the number of side detectors. In 2022, Milton analyses and compares the use and benefits of several combining schemes to create diversity at the optical receiver in a multi-cell indoor VLC system. The results indicates that the ADR implemented with the maximum-ratio combining (MRC) scheme outperforms the other schemes, such as equal gain combining (EGC) and selection best combining (SBC), in terms of SINR and User Data Rate [18]. In 2024, Al-Sakkaf derives theoretical expressions for the probability distribution function (PDF) and cumulative distribution function (CDF) of the SINR in multicell scenarios for ADRs, where the FOV generated by each PD may overlap with those of other PDs [20]. Recently, leveraging the advantages of off-axis FOV and freeform optics, a modified and compact-size ADR, known as the freeform diversity receiver (FDR), is first proposed in [21]. It is demonstrated that 120.5 dB average SINR can be attained over the communication floor. A further study of the FDR is conducted under conditions of light path blockage, considering multiple users with random mobility within a hybrid LiFi/WiFi network (HLWNet) [22]. Due to the lower channel correlation achieved from the angle diversity scheme, ADRs are introduced to improve the performance of indoor

massive multiple-input multiple-output (MIMO)-VLC systems, and the pyramid receivers (PRs) are proposed [25]. The generalised structure of truncated pyramid receivers (TPRs) are given in [26] to reduce the SINR fluctuation. In 2019, the work in [23] investigates the performance of two different MIMO modulation schemes - generalised spatial modulation (GSM) and spatial multiplexing (SMP) - for an VLC system using vertical and angular detectors. The results show that ADRs provide better bit error rate (BER) performance than vertical detectors. In 2021, Vipul proposed a MIMO-VLC system using an ADR with repetition coding at the transmitter and various receiver diversity schemes - MRC, EGC, and SBC - to enhance performance. The study derived closed-form expressions for the average error probability under imperfect channel state information (CSI) and found that increasing signal-to-noise-ratio (SNR) does not sufficiently mitigate the effects of high channel estimation errors [24]. In 2023, the ADR is used to propose a MIMO-VLC system employing L-pulse position modulation (L-PPM) [27].

Although many studies have been conducted on ADR in LiFi systems, the optimal ADR structure that simultaneously considers the impact of tilt angle, FOV, and the number of PDs has not yet been determined. As a result, the optimal configurations for ADRs are not provided, and the potential performance gains are not fully realised. Moreover, most of the systems are assumed to be interference limited instead of noise limited, which is not always true as the ADR can mitigate most of ICI with noise being the dominated part.

In addition, to obtain a more accurate evaluation of the system performance, the following three factors must be taken into consideration: (1) User Device Orientation Most of the studies on ADRs assume that the receiving device is pointed vertically upward. However, it has been shown in our previous works that the random orientation of mobile devices can significantly affect the direct current (DC) channel gain and thus the system performance [28,29]. Therefore, the random orientation of the user equipment (UE) needs to be considered. A random device orientation model has been proposed in [28]. This model will be applied in this study to evaluate the system more accurately.

(2) Diffuse Link Signal Propagation The non-line-of-sight (NLOS) link is neglected in most LiFi and VLC studies and only the LOS channel is considered [2,3,7,30]. In [31], it is shown that the LOS link is the dominate link and the effect of the reflected signal can be neglected. However, the UE is assumed to be positioned vertically upward, which is not realistic for mobile devices. In our study, we consider the effect of reflection when random device orientation is applied and the results show that the diffuse link cannot be ignored. A microscopic frequency-domain method for the simulation of the indoor VLC channel is presented in [32]. A closed form for the transfer function that contains all reflection orders is formulated. The method can be extended to multi-spot transmission without a significant increase in the computational complexity. Therefore, in this study, we will use the frequency-domain method to simulate the impact of the diffuse link.

(3) Noise Power Spectral Density The noise power spectral density of the PD has a huge impact on the analyses of system performance. For different levels of noise power spectral density, the system could be noise-limited, interference-limited or noise-plus-interference limited, which could affect the choices of the signal combining schemes and the cell configurations.

The main contributions of this paper are summarised as follows:

- The coverage area of ADRs is defined to differentiate from the coverage area of APs. Analytical expressions for the coverage area of both PRs and TPRs are given.
- Based on the constraint set by the coverage area of ADRs, the lower bound of FOV of PDs on an ADR is given for the single source (SS) system. The performances of PRs and TPRs are compared, and optimised ADR structures that simultaneously consider the impact of tilt angle, FOV, and the number of PDs are proposed to fully exploit the potential performance gains of ADRs. Additionally, the joint effect of receiver and transmitter bandwidth on the average data rate is analysed.

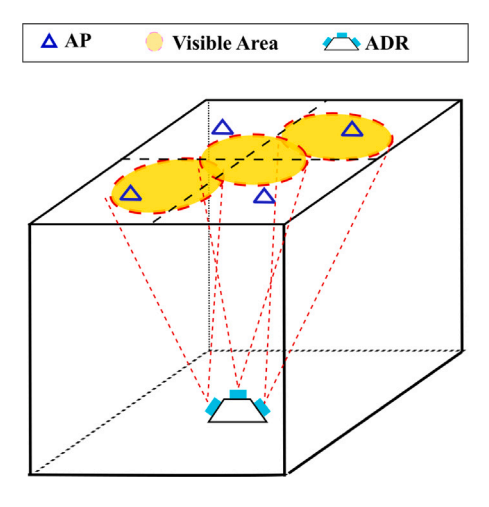


Fig. 1. System model

- The performance comparison between the SBC and MRC are given regarding different levels of noise power spectral density. It is the first time shown that under certain circumstances, the SBC can outperform the MRC.
- The double source (DS) cell system is considered to further mitigate the NLOS interference. The lower bound of FOV of PDs on an ADR is derived and the optimised ADR structures are proposed for the DS system.
- By comparing the average SINR between the DS system and the SS system under different levels of noise power spectral density, we present that, in a noise-dominated scenario, the SS system should be applied, otherwise, the DS system is preferred.

The rest of this paper is organised as follows. The system model is introduced in Section 2. The generalised structures of ADRs are given in Section 3. Section 4 presents the optimum FOV for PRs and TPRs. The concepts of the optical double-source cell are proposed in Section 5. The simulation results and discussions are presented in Section 6. Finally, conclusions are drawn in Section 7.

2. System model

As shown in Fig. 1, an indoor LiFi network is considered in this study, where $N_{\rm L}$ LiFi APs are deployed in the ceiling. On the receiver side, the ADR is utilised to collect the transmitted signal. In the following, the LiFi system model is described in details.

2.1. Light propagation model

In indoor optical communications, the signal propagation consists of two components: the LOS link and the diffuse link.

2.1.1. LOS link

It is typically assumed that the LED follows the Lambertian radiation pattern and the LOS DC channel gain between the transmitter (Tx) and receiver (Rx) is given by [1,8]:

$$H_{\text{LOS}} = \frac{(m+1)}{2\pi d^2} A_{\text{p}} T_s(\psi) g(\psi) \cos^m(\phi) \cos(\psi) v_{\text{Tx,Rx}}, \tag{1}$$

where m is the Lambertian order, which is given as $m=-\ln(2)/\ln(\cos(\Phi_{1/2}))$, and $\Phi_{1/2}$ denotes the half-power semi-angle of the LED; d is the distance between the Tx and the Rx; $A_{\rm p}$ denotes the physical area of the PD; $T_{\rm s}(\psi)$ represents the signal transmission gain of the optical filter; The irradiance angle of the transmitter is denoted as ϕ and the incidence angle of the receiving PD is denoted as ψ . Note that ψ can be obtained by $\cos(\psi) = \frac{{\bf n}_{\rm PD} \cdot {\bf d}}{\|{\bf d}\|}$, where ${\bf d}$ defines the distance vector between

the Tx and the Rx. The dot product is denoted as (\cdot) and $\|\mathbf{d}\|$ denotes the Euclidean distance. Furthermore, \mathbf{n}_{PD} is the normal vector of the PD. $g(\psi)$ is the concentrator gain and $g(\psi) = \frac{n_{\text{ref}}^2}{\sin^2(\Psi_c)}$, where n_{ref} represents the internal refractive index of the concentrator and Ψ_c denotes the FOV of the PD with concentrator. $v_{\text{Tx,Rx}}$ represents the visibility factor and is given by [32]:

$$v_{\mathrm{Tx,Rx}} = \begin{cases} 0, & \phi > \pi/2 \text{ or } \psi > \Psi_{\mathrm{c}} \\ 1 & \text{otherwise} \end{cases}$$
 (2)

2.1.2. NLOS link

The diffuse link is due to the reflection from the walls. As mentioned earlier, the frequency-domain method in [32] is used to obtain the diffuse link DC channel gain. We assume that all the wall surfaces are purely diffuse Lambertian reflectors with m = 1. All of the surfaces are divided into a number of small surface elements numbered by $k = 1, ..., N_E$, with areas A_k and reflective coefficients ρ_k . To calculate the diffuse link DC channel gain, the propagation of light is divided into the following three parts. The first part of the diffuse link propagation is the light path between the Tx and all the reflective surface elements of the room. The LOS DC channel gain between the Tx and the surface element k is defined as $H_{Tx,k}$. The transmitter transfer vector, \mathbf{t} , is defined as $\mathbf{t} = (H_{\mathrm{Tx},1}, \ H_{\mathrm{Tx},2}, \ \dots \ H_{\mathrm{Tx},N_{\mathrm{E}}})^{\mathrm{T}}$, where $(\cdot)^T$ defines the transpose of vectors. The second part of the diffuse link is the LOS link from all the $N_{\rm E}$ surface elements to all the $N_{\rm E}$ surface elements. The LOS DC channel gain between the surface elements k and the surface element i is given as $H_{k,i}$. To describe the LOS links between all surfaces inside the room, the $N_{\rm E} \times N_{\rm E}$ room-intrinsic transfer matrix, **H**, is defined by its elements $[\mathbf{H}]_{k,i} = H_{k,i}$. In order to include the reflective coefficient ρ_k of the surface elements, the $N_E \times N_E$ reflectivity matrix is defined as $G_{\rho} = \operatorname{diag}(\rho_1, \rho_2, \dots, \rho_{N_{\mathrm{E}}})$ [32]. In the third part of the diffuse link, the light propagates from all the surfaces of the room to the Rx. Similarly, we denote the LOS DC channel gain between the surface element k and the Rx as $H_{k,Rx}$. The LOS DC channel gain between all the reflective elements of the room and the receiver are grouped to give the receiver transfer vector ${\bf r}$ which is defined by its transpose $\mathbf{r}^{\mathrm{T}}=(H_{1,\mathrm{Rx}},\ H_{2,\mathrm{Rx}},\ ...\ H_{N_{\mathrm{E}},\mathrm{Rx}})$. Therefore, the total diffuse DC channel gain with infinite reflection can be calculated by the matrix product [32]:

$$H_{\text{diff}} = \mathbf{r}^{\mathrm{T}} \mathbf{G}_{\rho} (\mathbf{I} - \mathbf{H} \mathbf{G}_{\rho})^{-1} \mathbf{t}, \tag{3}$$

where I denotes the unity matrix.

2.2. Signal combining schemes for ADR

An indoor LiFi network is studied and it is assumed that the total number of UE and LiFi APs are N_{UE} and N_{L} , respectively. The set of APs is denoted by $A = \{\alpha \mid \alpha \in [1, N_L]\}$. The set of users is denoted as $\mathcal{U} = \{ \mu \mid \mu \in [1, N_{\text{UE}}] \}$. The ADR is used as the Rx and the set of PDs on an ADR is denoted as $P = \{p \mid p \in [1, N_{PD}]\}$, where $N_{\rm PD}$ denotes the total number of PDs on the ADR. As one of the most commonly used optical orthogonal frequency division multiplexing (O-OFDM) schemes, the direct current biased optical OFDM (DCO)-OFDM is used in this study as it is spectrum efficient [33]. The number of OFDM subcarriers is denoted as M, where M is an even and positive integer, and the sequence number of OFDM subcarriers is denoted by $m \in \{0, 1, ..., M-1\}$. Two constraints should be satisfied to ensure real and positive signals: (i) X(0) = X(M/2) = 0, and (ii) the Hermitian symmetry constraint, i.e., $X(m) = X^*(M-m)$, for $m \neq 0$, where $(\cdot)^*$ denotes the complex conjugate operator [31]. Therefore, the effective subcarrier set bearing information data is defined as $\mathcal{M}_e = \{m | m \in \mathbb{N}\}$ $[1, M/2 - 1], m \in \mathbb{N}$, where \mathbb{N} is the set of natural numbers.

For an ADR, multiple PDs are receiving signals simultaneously. Thus, attention should be paid to the selection of the signal combining schemes. There are different combining schemes such as equal gain combining (EGC), SBC and MRC. An important metric to evaluate the

link quality and capacity is the SINR. The SINR of user μ on subcarrier m can be obtained based on [9,31]:

$$\begin{split} \gamma_{\mu,m} &= \frac{(\sum_{p=1}^{N_{\text{PD}}} \tau P_{\text{tx}} w_p H_{\alpha_s,\mu,p})^2 / (M-2)}{\sum_{p=1}^{N_{\text{PD}}} w_p^2 \kappa^2 N_0 B_{\text{L}} / M + \sum_{\alpha_i \in \mathcal{A} \backslash \{\alpha_s\}} (\tau P_{\text{tx}} \sum_{p=1}^{N_{\text{PD}}} w_p H_{\alpha_i,\mu,p})^2 / (M-2)}{(\sum_{p=1}^{N_{\text{PD}}} \tau P_{\text{tx}} w_p H_{\alpha_s,\mu,p})^2}, \quad (4) \\ &= \frac{(\sum_{p=1}^{N_{\text{PD}}} \tau P_{\text{tx}} w_p H_{\alpha_s,\mu,p})^2}{\sum_{p=1}^{N_{\text{PD}}} w_p^2 \kappa^2 N_0 B_{\text{L}} (M-2) / M + \sum_{\alpha_i \in \mathcal{A} \backslash \{\alpha_s\}} (\tau P_{\text{tx}} \sum_{p=1}^{N_{\text{PD}}} w_p H_{\alpha_i,\mu,p})^2} \end{split}$$

where τ is the optical-to-electrical conversion efficiency; $P_{\rm Ix}$ is the transmitted optical power of the AP; w_p denotes the combining weight of PD p; $H_{\alpha_s,\mu,p}$ is the overall DC channel gain between the PD p of user μ and the serving AP α_s ; κ is the ratio of DC optical power to the square root of electrical signal power; N_0 represents the noise power spectral density of the additive white Gaussian noise and $B_{\rm L}$ is the baseband modulation bandwidth; $H_{\alpha_i,\mu,p}$ is the overall DC channel gain between the PD p of user μ and the interfering LiFi AP α_i . The serving AP a_s for user μ is selected based on the signal strength strategy (SSS) where the UEs are connected to the APs providing the best received signal strength. Hence, the serving AP α_s for user μ can be expressed as:

$$\alpha_{\rm s} = \underset{\alpha \in \mathcal{A}}{\arg \max} \sum_{p=1}^{N_{\rm PD}} |H_{\alpha,\mu,p}|^2. \tag{5}$$

When the EGC scheme is adopted, the signals received by the PDs are simply combined with equal weights, which can be described as:

$$w_p = 1$$
, for any $p \in \mathcal{P}$. (6)

In terms of the SBC scheme, a switch circuit is required to output the information from the PD with the highest SINR. Hence, the weight of each PD is given as:

$$w_p = \begin{cases} 1, & p = p_{s} \\ 0, & \text{otherwise,} \end{cases}$$
 (7)

where p_s can be obtained by:

$$p_{\rm s} = \mathop{\rm arg\,max}_{p\in\mathcal{P}} \frac{(\tau P_{\rm tx} H_{\alpha_{\rm s},\mu,p})^2}{\kappa^2 N_0 B_{\rm L}(M-2)/M + \sum_{\alpha_{\rm i}\in\mathcal{A}\setminus\{\alpha_{\rm s}\}} (\tau P_{\rm tx} H_{\alpha_{\rm i},\mu,p})^2}. \tag{8}$$

On the subject of the MRC schemes, the weight for each PD is denoted as [9]:

$$w_p = \frac{(\tau P_{\text{tx}} H_{\alpha_s, \mu, p})^2}{\kappa^2 N_0 B_{\text{L}}(M - 2)/M + \sum_{\alpha: \in A \setminus \{\alpha_s\}} (\tau P_{\text{tx}} H_{\alpha_s, \mu, p})^2}.$$
 (9)

Based on the Shannon capacity, assuming electrical signals after optical to electrical conversion, the data rate of the μ th UE on subcarrier m can be expressed:

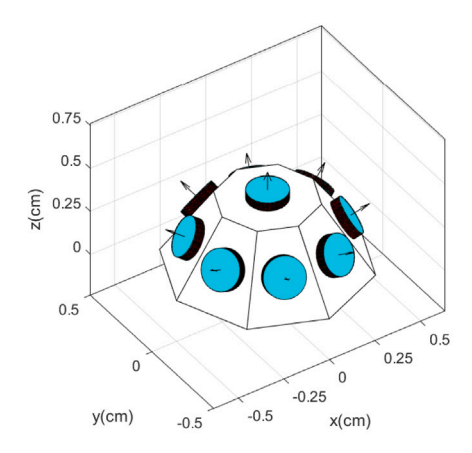
$$\zeta_{\mu,m} = \begin{cases} \frac{B_{L}}{M} \log_{2}(1 + \gamma_{\mu,m}), & m \in [1, M/2 - 1] \\ 0, & \text{otherwise} \end{cases}$$
 (10)

$$\begin{aligned} &(x_{\text{PD},p}, y_{\text{PD},p}, z_{\text{PD},p}) \\ &= \begin{cases} \left(x_{\text{UE}} + r\cos\frac{2(p-1)\pi}{N_{\text{TPR}}-1}, \ y_{\text{UE}} + r\sin\frac{2(p-1)\pi}{N_{\text{TPR}}-1}, \ z_{\text{UE}}\right), & \text{if } 1 \leq p < N_{\text{TPR}} \\ (x_{\text{UE}}, \ y_{\text{UE}}, \ z_{\text{UE}}), & & \text{if } p = N_{\text{TPR}} \end{cases} \end{aligned}$$

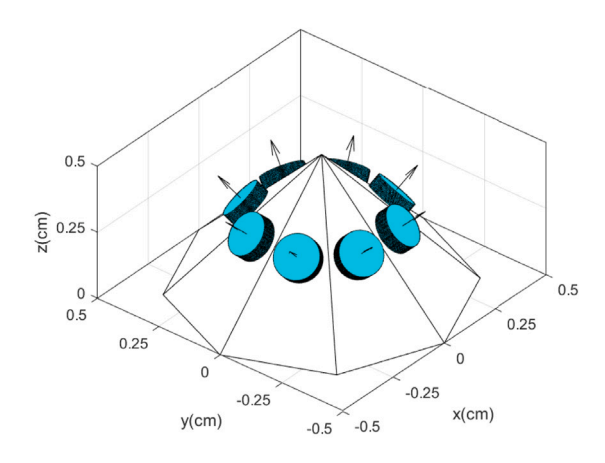
Hence, the data rate of the $\mu{\rm th}$ UE can be obtained by $\zeta_{\mu}\!=\!\sum_{m=1}^{M/2-1}\zeta_{\mu,m}$

3. ADR structure

The ADR is composed of multiple PDs facing in different directions. By using a PD in conjunction with a compound parabolic concentrator (CPC), a narrow FOV and high optical gain can be achieved [8]. However, the narrow FOV is achieved at the expense of the longer length of the CPC. Therefore, the number of PDs on the ADR should be limited



(a) The structure of TPR with $N_{\text{TPR}} = 9$.



(b) The structure of PR with $N_{PR} = 8$.

Fig. 2. ADR structures.

due to the size limitation on the mobile devices and smartphones. In this study, the TPR [26] and the PR [25] are considered as they are both suitable for hand-held devices. The number of PDs on the TPR and PR are separately denoted as $N_{\rm TPR}$ and $N_{\rm PR}$. The structure of the TPR with $N_{\rm TPR}=9$ and the PR with $N_{\rm PR}=8$ are presented in Figs. 2(a) and 2(b), respectively. The ADR designs are analysed in the following parts.

3.1. TPR design

The TPR is composed of a central PD and a ring of $N_{\rm TPR}-1$ equally separated side PDs. The side PDs are arranged uniformly in a circle of radius r on the horizontal plane. Thus, the coordinate of the pth PD on a TPR is represented as (11), where $(x_{\rm UE}, y_{\rm UE}, z_{\rm UE})$ is the UE position, denoted as ${\bf p}_{\rm UE}$ [11]. As the distance between the AP and the UE is much larger than r, the distances between the AP and all PDs on a TPR are approximately the same. The normal vector of each PD can be described by two angles: the azimuth angle of a PD, $\omega_{\rm PD}$, and the elevation angle of a PD, $\theta_{\rm PD}$ [10]. When the UE is pointing vertically upward, the TPR has one vertically orientated central PD and $N_{\rm TPR}-1$ inclined side PDs with identical elevation angles $\Theta_{\rm PD}$. In other words, the elevation angle of the pth PD on a TPR can be expressed as:

$$\theta_{\text{PD,vert},p} = \begin{cases} \Theta_{\text{PD}}, & \text{if } 1 \le p < N_{\text{TPR}} \\ 0, & \text{if } p = N_{\text{TPR}} \end{cases}$$
 (12)

The azimuth angle of the pth PD is given by:

$$\omega_{\text{PD,vert},p} = \begin{cases} \frac{2(p-1)\pi}{N_{\text{TPR}}-1}, & \text{if } 1 \le p < N_{\text{TPR}} \\ 0, & \text{if } p = N_{\text{TPR}} \end{cases}$$
 (13)

3.2. PR design

The PR can be regarded as a TPR without the central PD. Therefore, the coordinate of the *p*th PD on a PR is given by:

$$(x_{\text{PD},p}, y_{\text{PD},p}, z_{\text{PD},p}) = \left(x_{\text{UE}} + r\cos\frac{2(p-1)\pi}{N_{\text{PR}}}, y_{\text{UE}} + r\sin\frac{2(p-1)\pi}{N_{\text{PR}}}, z_{\text{UE}}\right).$$
(14)

When the UE is vertically orientated, the elevation angle and the azimuth angle of the pth PD are separately expressed as:

$$\theta_{\text{PD,vert},p} = \Theta_{\text{PD}}, \quad \omega_{\text{PD,vert},p} = \frac{2(p-1)\pi}{N_{\text{PR}}}.$$
 (15)

3.3. Random orientation model

The orientation of a UE has a great impact on the channel DC gain according to (1). In [28], a model for the random orientation of mobile devices based on experiments is proposed so that the system performance of LiFi attocell networks can be evaluated more accurately. The random orientation model can be described by two angles: the elevation angle of a UE, $\theta_{\rm UE}$, and the azimuth angle of a UE, $\omega_{\rm UE}$. The geometrical representation of $\theta_{\rm UE}$ and $\omega_{\rm UE}$ is manifested in Fig. 3. The probability density function (PDF) of $\theta_{\rm UE}$ can be modelled as the truncated Laplace distribution and it can be simplified as [28]:

$$f_{\theta}(\theta_{\mathrm{UE}}) \cong \frac{\exp(-\frac{|\theta_{\mathrm{UE}} - \mu_{\theta}|}{b_{\theta}})}{2b_{\theta}}, \quad 0 \le \theta \le \frac{\pi}{2}, \tag{16}$$

$$\mathbf{n}_{\mathrm{UE}} = \mathbf{R}\omega_{\mathrm{UE}}\mathbf{R}(\theta_{\mathrm{UE}})\mathbf{n}_{\mathrm{UE,vert}} = \left[\sin\theta_{\mathrm{UE}}\cos\omega_{\mathrm{UE}}, \sin\theta_{\mathrm{UE}}\sin\omega_{\mathrm{UE}}, \cos\theta_{\mathrm{UE}}\right]^{\mathrm{T}}$$
(17)

where $b_{\theta} = \sqrt{\sigma_{\theta}^2/2}$. The mean and scale parameters are set as $\mu_{\theta} = 41.39^{\circ}$ and $\sigma_{\theta} = 7.68^{\circ}$ [28]. In addition, the PDF of the azimuth angle of a UE, ω_{UE} , is modelled as a uniform distribution. It is assumed that the UE is initially pointing vertically upward and $\mathbf{n}_{\text{UE},\text{vert}} = [0,0,1]^{\text{T}}$. The normal vector of the UE after rotation becomes \mathbf{n}_{UE} . The rotation can be simplified as rotating around the y-axis with θ_{UE} and then rotating around z-axis with ω_{UE} , which can be described by rotation matrices $\mathbf{R}(\theta_{\text{UE}})$ and $\mathbf{R}(\omega_{\text{UE}})$ separately [34]. Thus, \mathbf{n}_{UE} is given by (17).

3.4. Normal vector of the ADR

When the UE is pointing vertically upward, for both PRs and TPRs, the normal vector of the pth PD is obtained as:

$$\mathbf{n}_{\text{PD,vert},p} = \begin{bmatrix} \sin(\theta_{\text{PD,vert},p})\cos(\omega_{\text{PD,vert},p}) \\ \sin(\theta_{\text{PD,vert},p})\sin(\omega_{\text{PD,vert},p}) \\ \cos(\theta_{\text{PD,vert},p}) \end{bmatrix}. \tag{18}$$

However, the normal vector of the UE will change due to the random rotation. The random orientation model is described in Section 3.3. Thus, the normal vector of the pth PD after the random rotation is obtained by:

$$\begin{aligned} \mathbf{n}_{\text{PD},p}(\theta_{\text{UE}}, \omega_{\text{UE}}) &= \mathbf{R}(\omega_{\text{UE}}) \mathbf{R}(\theta_{\text{UE}}) \mathbf{n}_{\text{PD,vert},p} \\ &= \begin{bmatrix} C_1 \cos \omega_{\text{UE}} \cos \theta_{\text{UE}} - C_2 \sin \omega_{\text{UE}} + \sin \theta_{\text{UE}} \cos \omega_{\text{UE}} \cos(\theta_{\text{PD,vert},p}) \\ C_1 \sin \omega_{\text{UE}} \cos \theta_{\text{UE}} + C_2 \cos \omega_{\text{UE}} + \sin \theta_{\text{UE}} \sin \omega_{\text{UE}} \cos(\theta_{\text{PD,vert},p}) \\ -C_1 \sin \theta_{\text{UE}} + \cos \theta_{\text{UE}} \cos(\theta_{\text{PD,vert},p}) \end{bmatrix}, \end{aligned}$$

$$(19)$$

where $C_1 = \sin(\theta_{\text{PD,vert},p})\cos(\omega_{\text{PD,vert},p})$ and $C_2 = \sin(\theta_{\text{PD,vert},p})\sin(\omega_{\text{PD,vert},p})$. Based on (19), after the random rotation, the elevation angle of the pth PD can be obtained as:

$$\theta_{\text{PD},p} = \cos^{-1} \left(-C_1 \sin \theta_{\text{UE}} + \cos \theta_{\text{UE}} \cos \theta_{\text{PD,vert},p} \right), \tag{20}$$

$$\omega_{\text{PD},p} = \tan^{-1} \left(\frac{C_1 \sin \omega_{\text{UE}} \cos \theta_{\text{UE}} + C_2 \cos \omega_{\text{UE}} + \sin \theta_{\text{UE}} \sin \omega_{\text{UE}} \cos(\theta_{\text{PD,vert},p})}{C_1 \cos \omega_{\text{UE}} \cos \theta_{\text{UE}} - C_2 \sin \omega_{\text{UE}} + \sin \theta_{\text{UE}} \cos \omega_{\text{UE}} \cos(\theta_{\text{PD,vert},p})} \right)$$
(21)

and the azimuth angle of the *p*th PD can be expressed as (21). Therefore, the incidence angle of the *p*th PD, ψ_p , can be obtained based on $\theta_{\text{PD},p}$ and $\omega_{\text{PD},p}$ as $\psi_p = \cos^{-1}(\frac{\mathbf{n}_{\text{PD}}\cdot\mathbf{d}}{\|\mathbf{d}\|})$.

3.5. Receiver bandwidth vs PD area

The bandwidth of a PD is affected by its physical area, $A_{\rm p}$, and the PD thickness, $L_{\rm p}$. The capacitance of the each PD is denoted as $C_{\rm r}=\varepsilon_0\varepsilon_{\rm r}\frac{A_{\rm p}}{L_{\rm p}}$, where ε_0 and $\varepsilon_{\rm r}$ are the permittivity of vacuum and the relative permittivity of silicon, respectively. The load resistance is defined as $R_{\rm load}$ while the hole velocity is denoted as $v_{\rm p}$. Therefore, the receiver bandwidth can be written as [35]:

$$B_{\rm r} = \frac{1}{\sqrt{(2\pi R_{\rm load} C_{\rm r})^2 + \left(\frac{L_{\rm p}}{0.443v_{\rm p}}\right)^2}}.$$
 (22)

By solving $\frac{\partial B_r}{\partial L_p}=0$, the optimum L_p can be denoted as $L_{p,\mathrm{opt}}=\sqrt{0.886\pi R_{\mathrm{load}} \epsilon_0 \epsilon_r A_p \nu_p}$.

3.6. Visibility of an ADR

The visibility of an ADR was first defined in [10]. An AP is visible to a PD when the AP is within the FOV of the PD. Hence, at the location \mathbf{p}_{UE} and the orientation ($\theta_{\mathrm{UE}}, \omega_{\mathrm{UE}}$), the visibility factor between the pth PD on the ADR and the α th AP can be expressed as:

$$v_{\alpha,p}(x_{\mathrm{UE}}, y_{\mathrm{UE}}, \theta_{\mathrm{UE}}, \omega_{\mathrm{UE}}, \Psi_{\mathrm{c}}) = \begin{cases} 0, & \psi_{\alpha,p} > \Psi_{\mathrm{c}} \\ 1, & \text{otherwise,} \end{cases}$$
and
$$\psi_{\alpha,p} = \arccos\left(\frac{\mathbf{n}_{\mathrm{PD},p}(\theta_{\mathrm{UE}}, \omega_{\mathrm{UE}}) \cdot \mathbf{d}_{\alpha}}{\|\mathbf{d}_{\alpha}\|}\right),$$
(23)

where $\mathbf{d}_{\alpha} = (x_{\alpha} - x_{\mathrm{UE}}, y_{\alpha} - y_{\mathrm{UE}}, z_{\alpha} - z_{\mathrm{UE}})$ is the distance vector between the AP α and the UE. The dot product is denoted as (\cdot) and $\|\cdot\|$ is the norm operator. In terms of ADR, an AP is visible to an ADR if and only if the AP is visible to at least one of the PDs on the ADR. Hence, for a given UE position and orientation, the visibility of the ADR can be written as [10]:

$$V(x_{\mathrm{UE}}, y_{\mathrm{UE}}, \theta_{\mathrm{UE}}, \omega_{\mathrm{UE}}, \Psi_{\mathrm{c}}) = \begin{cases} 1, & \text{if } \sum_{\alpha \in \mathcal{A}} \sum_{p \in \mathcal{P}} v_{\alpha, p} \neq 0 \\ 0, & \text{otherwise.} \end{cases}$$
 (24)

$$p_{v}(\boldsymbol{\Psi}_{c}) = \int_{x_{\text{UE}}} \int_{y_{\text{UE}}} \int_{\theta_{\text{UE}}} \int_{\omega_{\text{UE}}} V(x_{\text{UE}}, y_{\text{UE}}, \theta_{\text{UE}}, \omega_{\text{UE}}, \boldsymbol{\Psi}_{c})$$

$$= \frac{1}{X_{\text{UE}}} \frac{1}{Y_{\text{UE}}} \frac{1}{\Omega_{\text{UE}}} f_{\theta}(\theta_{\text{UE}}) dx_{\text{UE}} dy_{\text{UE}} d\theta_{\text{UE}} d\omega_{\text{UE}}$$

$$= \int_{x_{\text{UE}}} \int_{y_{\text{UE}}} \int_{\theta_{\text{UE}}} \int_{\omega_{\text{UE}}} \frac{V(x_{\text{UE}}, y_{\text{UE}}, \theta_{\text{UE}}, \omega_{\text{UE}}, \boldsymbol{\Psi}_{c})}{X_{\text{UE}} Y_{\text{UE}} \Omega_{\text{UE}}}$$

$$= \int_{\theta} \int_{$$

It is assumed that both $x_{\rm UE}$ and $y_{\rm UE}$ follow a uniform distribution. The probability of visibility of an ADR is defined as the probability that there is at least one AP within the visible area of the ADR for all UE positions and orientations, and it can be expressed as (25), where $X_{\rm UE}$, $Y_{\rm UE}$ and $\Omega_{\rm UE}$ are the range of $x_{\rm UE}$, $y_{\rm UE}$ and $\omega_{\rm UE}$, respectively. Hence, it can be obtained that $X_{\rm UE} = \max(x_{\rm UE}) - \min(x_{\rm UE})$, $Y_{\rm UE} = \max(y_{\rm UE}) - \min(y_{\rm UE})$ and $\Omega_{\rm UE} = \max(\omega_{\rm UE}) - \min(\omega_{\rm UE})$.

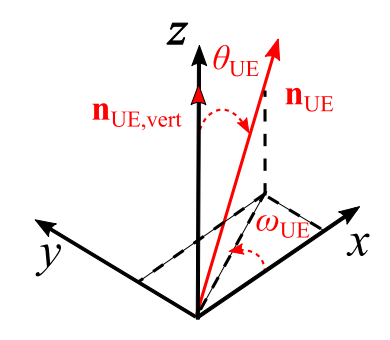
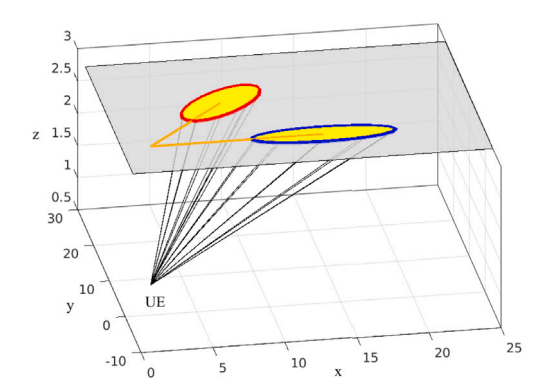
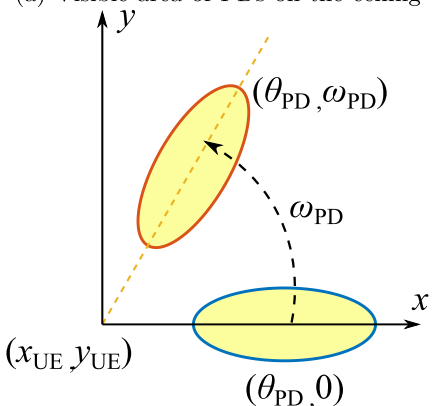


Fig. 3. Representation of random UE orientation.



(a) Visible area of PDs on the ceiling



(b) Representation of the visible area on the xy-plane.

Fig. 4. Visible area of PDs.

4. The optimum field of view

4.1. Optimisation problem

In (1), the LOS channel gain $H_{\rm LOS}$ is a convex function of $\Psi_{\rm c}$ and decreases monotonically. Hence, the smaller the $\Psi_{\rm c}$, the higher the channel gain. However, when the $\Psi_{\rm c}$ of the PD is too small, there is a high chance that no APs are visible to the ADR and the LOS link cannot be constructed. Thus, there is a trade off between the LOS channel gain and visibility. The optimisation problem is formulated as maximising the LOS channel gain based on the constraint that the ADR should provide visibility for all UE locations. Thus, the optimisation function is written as:

$$\operatorname*{arg\,max}_{\Psi_{\rm c}} \ H_{\rm LOS}(\Psi_{\rm c}),$$
 subject to $p_{\rm v}(\Psi_{\rm c})=1.$

The solution set of $p_{\rm v}(\Psi_{\rm c})=1$ is denoted as $\mathbb R$ and $\Psi_{\rm c,min}$ is the minimum value in $\mathbb R$. As $H_{\rm LOS}(\Psi_{\rm c})$ is a monotonically decreasing function, the maximum $H_{\rm LOS}(\Psi_{\rm c})$ is achieved when $\Psi_{\rm c}=\Psi_{\rm c,min}$. Hence, the optimisation problem can be solved by finding the minimum value of $\Psi_{\rm c}$, $\Psi_{\rm c,min}$, which satisfies $p_{\rm v}=1$. Based on (25), $\Psi_{\rm c,min}$ cannot be solved in a closed form. Therefore, in the following parts, we will study the ADRs' visible area on the ceilings to solve the solution set $\mathbb R$ and find a closed form for $\Psi_{\rm c,min}$.

4.2. Coverage area of ADR on the ceiling

The coverage area of a PR for a vertical-orientated UE is studied in [10]. Fig. 4(a) demonstrates that the visible area of the PD mounted on the PR is an ellipse on the ceiling. Hence, the visible area of the 1-st PD, where $\theta_{\rm PD,1} = \Theta_{\rm PD}$ and $\omega_{\rm PD,1} = 0$, is given by [10]:

$$\frac{(x_{\text{ellipse},1} - x_{\text{center}})^2}{a^2} + \frac{(y_{\text{ellipse},1} - y_{\text{center}})^2}{b^2} = 1,$$
(27)

whore

$$a = \frac{h\sin(2\Psi_{\rm c})}{\cos(2\Psi_{\rm c}) + \cos(2\Theta_{\rm PD})}, \quad b = \frac{\sqrt{2}h\sin(\Psi_{\rm c})}{\sqrt{\cos(2\Psi_{\rm c}) + \cos(2\Theta_{\rm PD})}},$$
 (28)

and

$$x_{\text{center}} = x_{\text{UE}} + \frac{h \sin(2\Theta_{\text{PD}})}{\cos(2\Psi_{\text{c}}) + \cos(2\Theta_{\text{PD}})}, \quad y_{\text{center}} = y_{\text{UE}}, \tag{29}$$

where h is the vertical distance between the AP and UE. The detailed proof is given in Appendix A. Fig. 4(b) depicts that the shape of the visible area of the pth PD can be obtained by rotating the 1-st PD around $(x_{\rm UE}, y_{\rm UE})$ with an angle of $\omega_{\rm PD,p}$, which can be represented as:

$$\begin{bmatrix} x_{\text{ellipse},p} - x_{\text{UE}} \\ y_{\text{ellipse},p} - y_{\text{UE}} \end{bmatrix} = R_{xy}(\omega_{\text{PD},p}) \begin{bmatrix} x_{\text{ellipse},1} - x_{\text{UE}} \\ y_{\text{ellipse},1} - y_{\text{UE}} \end{bmatrix} = \\ \begin{bmatrix} \cos \omega_{\text{PD},p} & -\sin \omega_{\text{PD},p} \\ \sin \omega_{\text{PD},p} & \cos \omega_{\text{PD},p} \end{bmatrix} \begin{bmatrix} x_{\text{ellipse},1} - x_{\text{UE}} \\ y_{\text{ellipse},1} - y_{\text{UE}} \end{bmatrix}.$$
(30)

$$\begin{bmatrix} x_{\text{ellipse},p} \\ y_{\text{ellipse},p} \end{bmatrix} = \begin{cases} \begin{bmatrix} \cos \omega_{\text{PD},p} & -\sin \omega_{\text{PD},p} \\ \sin \omega_{\text{PD},p} & \cos \omega_{\text{PD},p} \end{bmatrix} \\ \begin{bmatrix} x_{\text{ellipse},1} - x_{\text{UE}} \\ y_{\text{ellipse},1} - y_{\text{UE}} \end{bmatrix} + \begin{bmatrix} x_{\text{UE}} \\ y_{\text{UE}} \end{bmatrix}, & \text{if } 1 \le p < N_{\text{TPR}} \\ \end{bmatrix} \\ \begin{bmatrix} x_{\text{circle}} \\ y_{\text{circle}} \end{bmatrix}, & \text{if } p = N_{\text{TPR}} \end{cases}$$
(31)

The TPR can be seen as the combination of a PR, where $N_{\rm PR} = N_{\rm TPR} - 1$, and a central PD. When the UE is facing vertically upward, the visible area of the central PD is a circle. Therefore, the shape of the visible area of the *p*th PD on a TPR is given by (31), where $x_{\rm circle}^2 + y_{\rm circle}^2 = (h \tan \Psi_{\rm c})^2$.

4.3. Lower bound of FOV

For a fixed UE location, the ADR has the smallest coverage area on the ceiling when vertically orientated. In other words, we will investigate the worst condition, i.e. the situation that an ADR is positioned vertically upward which provides the smallest coverage area on the ceiling. Under other orientation scenarios, the coverage area is larger. Based on (30) and (31), Fig. 5 illustrates the visible area of 4 different types of ADRs when the UE is at the cell corner, that is to say, the cross-point of four LiFi cells. The blue curve is the outer boundary of the visible area. On the outer boundary, the points that have the shortest distance to the UE are defined as critical points, \mathbf{p}_{c} . d_{c} denotes the horizontal distance between \mathbf{p}_{c} and the UE. To ensure $p_{v}=1$, there

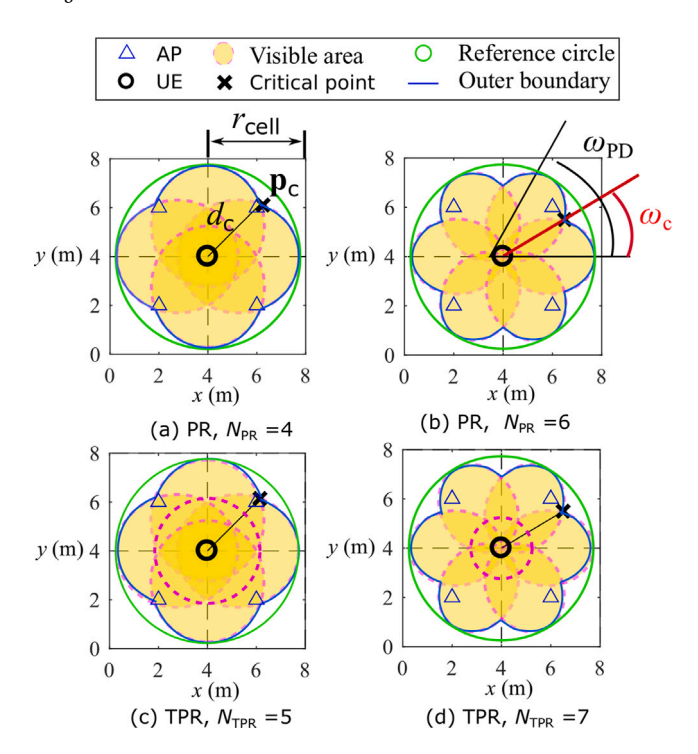


Fig. 5. Coverage area of PRs and TPRs with different number of PDs.

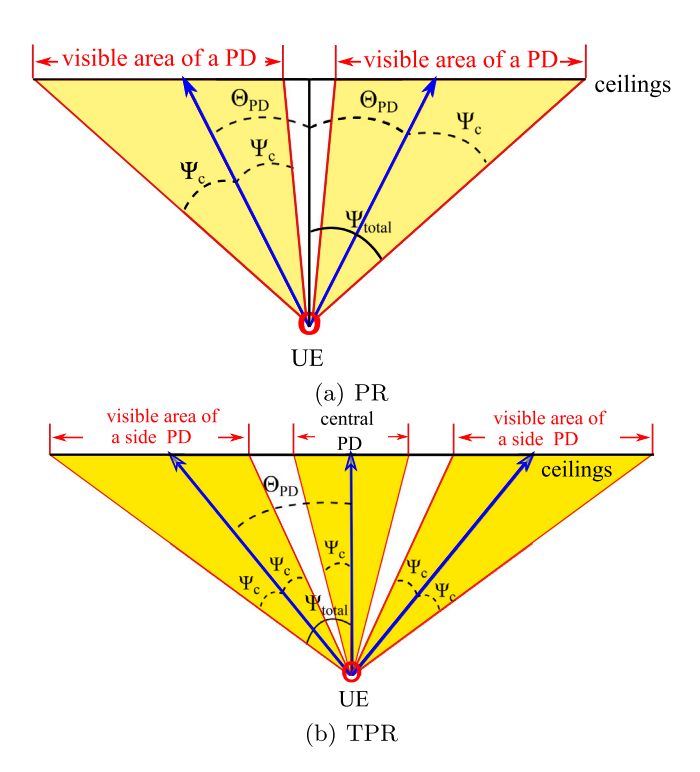


Fig. 6. Visible area of ADR in xz-plane.

are two constraints and the detailed explanation of these constraints are given as follows.

(1) Constraint I: The central area above the ADR should be visible to the ADR. As shown in Fig. 6(a), the total FOV of an ADR is represented as $\Psi_{\rm total}$, which can be written as:

$$\Psi_{\text{total}} = \Psi_{\text{c}} + \Theta_{\text{PD}}.\tag{32}$$

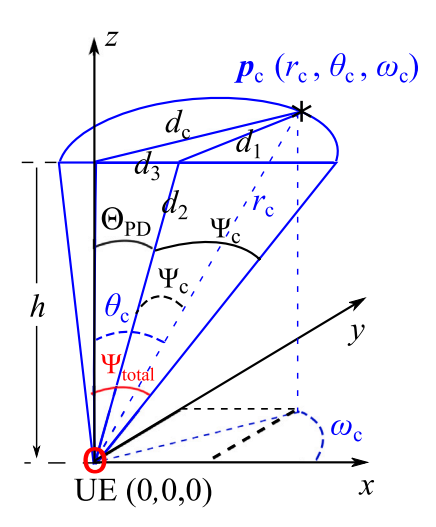


Fig. 7. The geometrical representation of $\Psi_{\rm c},~\Theta_{\rm PD},~\Psi_{\rm total}$ and $d_{\rm c}$ in the spherical coordinate system.

In terms of PRs, if $\Theta_{PD} \geq \Psi_c$, then the central part is not covered by the visible area of the ADR as manifested in Fig. 6(a). If the UE is in the cell centre, then no APs will be visible to the ADR. Hence, the condition $\Theta_{PD} \leq \Psi_c$ should be satisfied so that the area directly above the UE is covered by the visible area of the ADR. Based on this constraint and (32), the lower bound of Ψ_c can be obtained as:

$$\Psi_{\rm cl,min} = \frac{\Psi_{\rm total}}{2}.\tag{33}$$

With respect to the TPR, the area directly above the UE is covered by the central PD orientating vertically upwards as illustrated in Fig. 6(b). The concern should be the central coverage gap between the central PD and the side PDs. Therefore, $\Theta_{PD} \leq 2\Psi_c$ is required to ensure there is no gap between them. By substituting this constraint into (32), it can be derived that:

$$\Psi_{\rm cl,min} = \frac{\Psi_{\rm total}}{3}.\tag{34}$$

(2) Constraint II: The outer boundary of the visible area should be large enough. The side length of a square cell is denoted as $r_{\rm cell}$ as shown in Fig. 5. The horizontal distance between the UE and the α th AP is denoted as $d_{\rm h,\alpha}$. When the UE is at the cell corner, $d_{\rm h,\alpha} = \frac{\sqrt{2}}{2} r_{\rm cell}$ for any $\alpha \in \mathcal{A}$. With the decrease of $\mathcal{\Psi}_{\rm c}$, the outer boundary of the visible area will decrease, which means $d_{\rm c}$ will decrease. If $d_{\rm c}$ is smaller than the horizontal distance from the AP to the cell corner, which is $\frac{\sqrt{2}}{2} r_{\rm cell}$, there will be no APs within the visible area of the ADR for cell-corner users. Therefore, to ensure that at least one AP is visible to the cell-corner UE, $d_{\rm c}$ should be larger than the horizontal distance from the AP to the cell corner. By moving towards any direction, due to the symmetry, the cell-corner UE will get closer to at least one AP. In other words,

$$d_{\mathrm{c,min}} = \max_{x_{\mathrm{UE}},y_{\mathrm{UE}}} \left(\min_{\alpha} \left(d_{\mathrm{h},\alpha} \right) \right) = \frac{\sqrt{2}}{2} r_{\mathrm{cell}}, \text{ subject to } \alpha \in \mathcal{A}. \tag{35}$$

That is to say, if there is at least one AP inside the outer boundary of the visible area for the cell-corner UE, then, when the UE moves to other locations, the AP will still be inside the outer boundary of the visible area. Hence, to meet the condition $p_{\rm v}=1$, it is required that $d_{\rm c} \geq \frac{\sqrt{2}}{2} r_{\rm cell}.$ Also, it can be seen from Fig. 5 that ${\bf p}_{\rm c}$ is always inside the green reference circle, which has a radius of $h\tan(\Psi_{\rm total}).$ Hence, $d_{\rm c,min} \leq d_{\rm c} \leq h\tan(\Psi_{\rm total}),$ where $d_{\rm c,min} = \frac{\sqrt{2}}{2} r_{\rm cell}.$

Fig. 7 presents the geometrical relationship in a spherical coordinate system. The coordinate of $\mathbf{p}_{\rm c}$ is represented as $(r_{\rm c},\theta_{\rm c},\omega_{\rm c})$ and $\omega_{\rm c}=\frac{\omega_{\rm PD,p}}{2}|_{p=2}$ for both PRs and TPRs. The geometrical relationships among

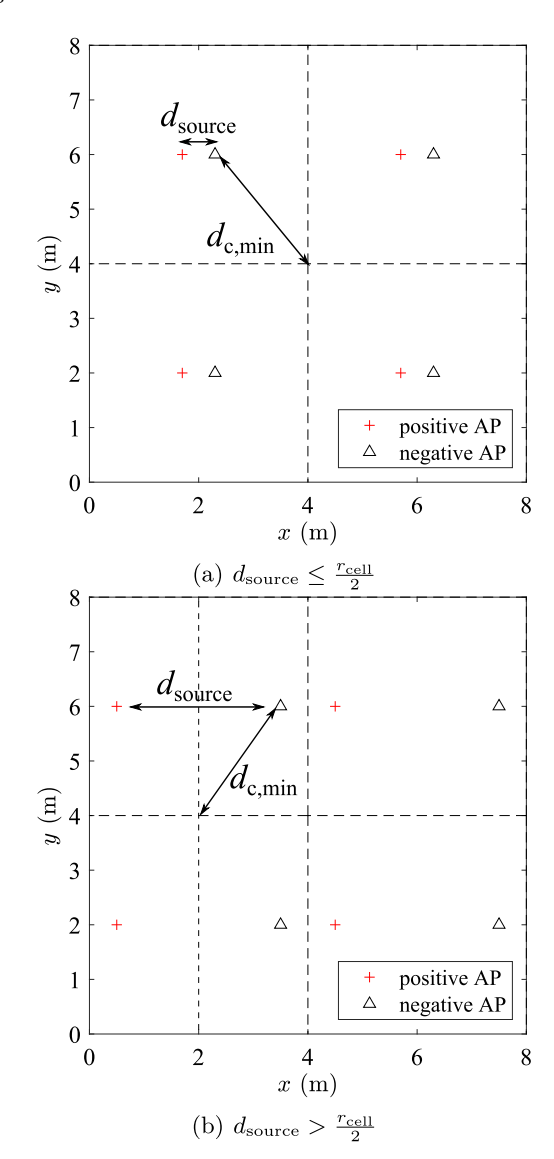


Fig. 8. Double source cell configuration.

 d_1, d_2 and d_3 , illustrated in Fig. 7, can be represented as:

$$d_1^2 = d_2^2 + r_c^2 - 2d_2r_c\cos(\Psi_c), \tag{36}$$

$$d_1^2 = d_3^2 + d_c^2 - 2d_3d_c\cos(\omega_c), \tag{37}$$

$$d_2^2 = h^2 + d_3^2$$
, $r_c^2 = h^2 + d_c^2$, $d_3 = h \tan(\Theta_{PD})$. (38)

According to (37), (36) and (38), the lower bound of Ψ_c set by Constraint II is derived in Appendix B and is represented as:

$$\Psi_{\rm c2,min} = \begin{cases} F_2(d_{\rm c2}), & \text{if } d_{\rm c,min} \le d_{\rm c2} \\ F_2(d_{\rm c,min}), & \text{otherwise} \end{cases} , \tag{39}$$

where

$$F_{2}(d_{c}) = \Psi_{\text{total}} - \tan^{-1} \frac{\sqrt{h^{2} + d_{c}^{2}} \cos(\Psi_{\text{total}}) - h}{d_{c} \cos(\omega_{c}) - \sqrt{h^{2} + d_{c}^{2}} \sin(\Psi_{\text{total}})},$$
(40)

and

$$d_{\rm c2} = \frac{h\cos(\omega_{\rm c})\sin(\Psi_{\rm total})}{\cos(\Psi_{\rm total}) + \sin(\omega_{\rm c})}.$$
 (41)

(3) Summary Based on (33), (34) and (39), the lower bound of $\Psi_{\rm c}$ can be expressed as:

$$\Psi_{c,\min} = \max(\Psi_{c1,\min}, \Psi_{c2,\min}). \tag{42}$$

Therefore, the solution set \mathbb{R} is $\Psi_{c,min} \leq \Psi_c \leq \Psi_{total}$. For different numbers of PDs on the PR, the optimum FOV is $\Psi_{c,min}$ as the FOV gets smaller, the higher the channel gain and received signal power.

5. Double source cell configuration

In the conventional SS cell configuration, each cell is equipped with a single AP in the cell centre. The double source (DS) cell configuration is proposed to further exploit the spatial diversity of the ADR in [36]. As demonstrated in Fig. 8, each LiFi AP consists of two sources which transmit the same information signals but with opposite polarity. These two sources are termed as the positive source and the negative source, which transmit the time domain signal $s_{\rm pos}(t)$ and $s_{\rm neg}(t)$ respectively. In a single optical cell, the received optical signal at a PD is denoted as [36]:

$$s_{\text{sum}}(t) = s_{\text{pos}}(t)H_{\text{pos}} + s_{\text{neg}}(t)H_{\text{neg}}, \tag{43}$$

where $H_{\rm pos}$ is the channel gain between the positive source and the PD; $H_{\rm neg}$ is the channel gain between the negative source and the PD. For a fair comparison, the total transmitting power for the SS system and DS system should be the same. Hence, the transmit power of each source is halved when the DS configuration is applied and the received optical power at the PD can be written as [36]:

$$P_{\rm rx} = \frac{P_{\rm tx}}{2} |H_{\rm pos} - H_{\rm neg}| = \frac{P_{\rm tx} \Delta H}{2}.$$
 (44)

Generally, the receiver is closer to the desired AP than the interfering AP. For the desired AP, due to the narrow FOV of ADRs, one PD can hardly receive LOS signals from both the positive source and negative source simultaneously, and only one appears as the LOS channel gain. In respect of the interfering AP, the channel gains $H_{\rm pos}$ and $H_{\rm neg}$ are both NLOS. Hence, the difference between $H_{\rm pos}$ and $H_{\rm neg}$ is small and the interference is attenuated accordingly. Therefore, the double source cell configuration can suppress the signal power from interfering APs [36]. As the LOS interference can be mitigated by the narrow FOV of the ADR and the NLOS interference can be mitigated due to the adoption of the DS configuration, the SINR of user μ on subcarrier m can be approximated by:

$$\tilde{\gamma}_{\mu,m} \approx \frac{(\sum_{p=1}^{N_{\rm PD}} w_p \tau \frac{P_{\rm tx}}{2} \Delta H_{\alpha_{\rm x},\mu,p})^2}{\sum_{n=1}^{N_{\rm PD}} w_p^2 \kappa^2 N_0 B_{\rm L}(M-2)/M},\tag{45}$$

$$\begin{split} d_{c,\min} &= \max_{x_{\text{UE}}, y_{\text{UE}}} \left(\min_{\alpha} (d_{\text{h},\alpha}) \right) \\ &= \begin{cases} \sqrt{\left(\frac{r_{\text{cell}}}{2} - \frac{d_{\text{source}}}{2} \right)^2 + \left(\frac{r_{\text{cell}}}{2} \right)^2}, & \text{if } d_{\text{source}} \leq \frac{r_{\text{cell}}}{2}}{2}, \\ \sqrt{\left(\frac{r_{\text{cell}}}{2} \right)^2 + \left(\frac{d_{\text{source}}}{2} \right)^2}, & \text{otherwise} \end{cases}, & \text{subject to } \alpha \in \mathcal{A}. \end{split}$$

where $\Delta H_{a_s,\mu,p}$ is the overall DC channel gain between the PD p of user μ and the serving AP a_s in the DS system. As manifested in Fig. 8, $d_{c,min}$ will vary according to the distance between the positive and negative sources, which can be represented as (46). Therefore, the lower bound of Ψ_c for the double source cell system can be calculated based on (39)–(42).

6. Results and discussions

6.1. Simulation setups

As shown in Fig. 5, an 8 m \times 8 m \times 3 m indoor office scenario is considered in this study, where 4 LiFi APs are deployed following a

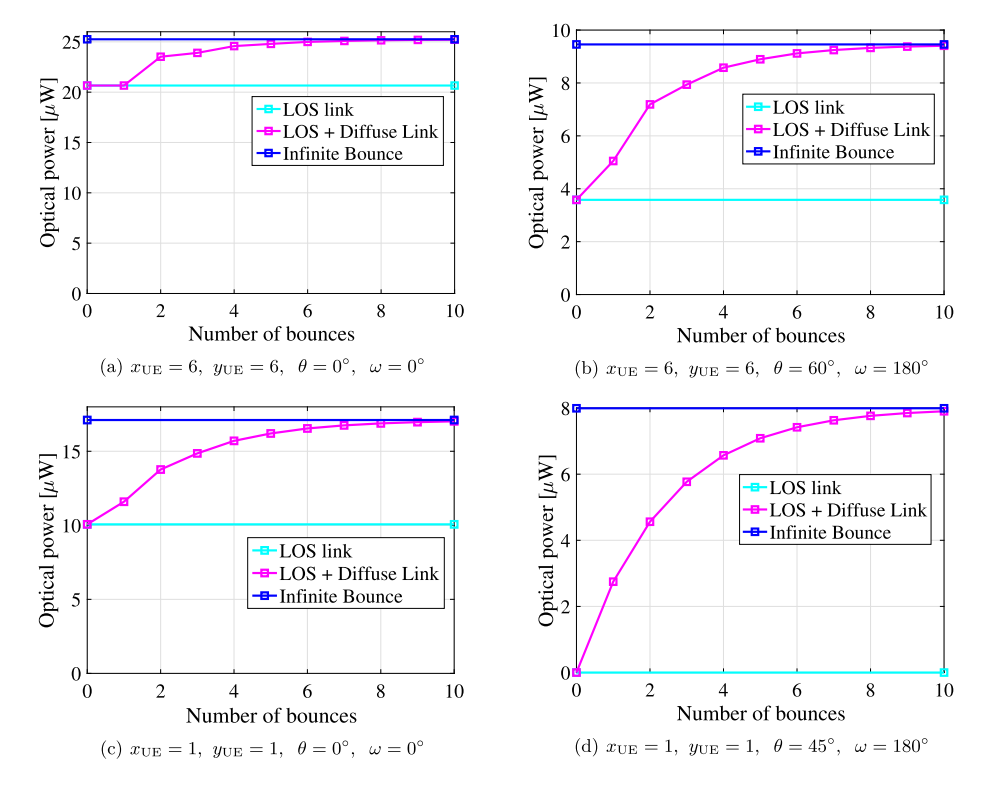


Fig. 9. Comparisons among received optical power for LOS link, LOS + diffuse link up to order L and infinite reflections in 2 different positions with different orientations.

Table 1 Parameters lists.

Transmitted optical power per AP	$P_{\rm tx}$	10 147
Transmitted optical power per in		10 W
Modulated bandwidth for LED	B	20 MHz
Physical are of the single PD receiver	$A_{\rm p}$	1 cm ²
FOV of the single PD receiver	Ψ_{c}^{r}	60°
The total FOV of an ADR	$\Psi_{ m total}$	60°
Half-intensity radiation angle	$\Phi_{1/2}$	60°
PD responsivity	τ	0.5 A/W
Noise power spectral density	N_0	$10^{-21} A^2/Hz$
Vertical distance between APs and UEs	h	2.15 m
Wall reflectivity	$ ho_{ m wall}$	0.8
Ceiling reflectivity	$ ho_{ m ceiling}$	0.8
Floor reflectivity	ρ_{floor}	0.3
Refractive index	n_{ref}	1.5
Optical filter gain	G	1
Permittivity of vacuum	ϵ_0	$8.854 \times 10^{-12} \text{ F m}^{-1}$
Relative permittivity of silicon	$\epsilon_{\rm r}$	11.68
Hole velocity	$v_{\rm p}$	$4.8 \times 10^4 \text{ m/s}$

square topology. All of the users are uniformly distributed in the room and move randomly following the random waypoint model [28]. To make a fair comparison, the total physical area, $A_{\rm t}=N_{\rm PD}A_{\rm p}$, of the ADRs should be the same. Hence, the physical area $A_{\rm p}$ on each PD decreases when the number of PDs increases. The other parameters used in the simulations are listed in Table 1.

6.2. Importance of reflection and orientation

Fig. 9 shows the received optical power in two different locations with different orientations. The room setup and the SS deployment is as shown in Fig. 6 and a single PD receiver with a FOV of 60° is used. The received optical power from the LOS and NLOS link can be calculated based on (1) and (3), respectively. The ratio of the received optical power from the LOS signal link to the total received optical power is represented as $p_{\rm los}$. In Figs. 9(a) and 9(b), the $p_{\rm los}$ of cell-centre

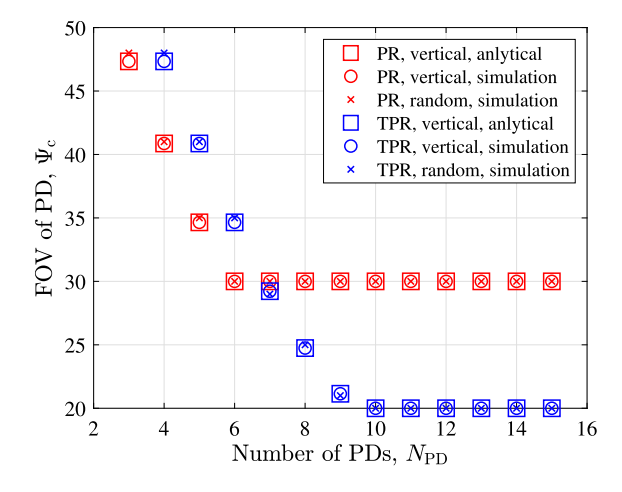


Fig. 10. The relationship between $\Psi_{\rm c,min}$ and the number of PDs, $N_{\rm PD}$, on an ADR for the SS system.

UEs at (6,6) degrades substantially when the orientation changes. In Fig. 9(c), the optical power from the diffuse link occupies more than 40% of the total optical power when $x_{\rm UE}=1$, $y_{\rm UE}=1$. Nevertheless, in Fig. 9(d), by changing the device orientation, there is no LOS signal and only the signal from the diffuse links can be received. Therefore, the device orientation has a great impact on the received single power and thus cannot be ignored. In addition, both the LOS link and diffuse link should be considered to analyse the performance of a multi-cell visible light communication system. Fig. 9 demonstrates that when the number of bounces is more than 5, the corresponding paths make a minor contribution to the total optical power. Hence, to reduce the computational complexity while maintaining high channel estimation accuracy, a light reflection order of L=5 and the orientation model proposed in [28] are considered for the following simulations.

6.3. Performance analysis for SS cells

(1) Lower bound of FOV: Fig. 10 manifests the relationship between the lower bound of the FOV, $\Psi_{\rm c,min}$, and the number of PDs. The analytical results are calculated based on the lower bound given in (42). The Monte-Carlo simulations for UEs with a vertical orientation can be carried out based on (25), and the lowest value of Ψ_c satisfying $p_v = 1$ is $\Psi_{\rm c,min}$. It can be seen that the analytical results exactly match the simulation results. When $N_{\rm PD} \leq$ 6, with the increase of $N_{\rm PD}$, $\Psi_{\rm c,min}$ decreases and the PR achieves smaller $\Psi_{\rm c,min}$ than the TPR. With the further increase of $N_{\rm PD}$ from 6 to 10, the lower bound of FOV, $\Psi_{\rm c.min}$, for the PR becomes fixed due to (33) while the $\Psi_{\rm c,min}$ for the TPR still decreases and is lower than the $\Psi_{\rm c,min}$ for the PR. For $N_{\rm PD} > 10$, $\Psi_{\rm c,min}$ does not change any more for TPR as well due to (34). It is noted that the Monte-Carlo simulations are also performed for UEs with the random orientation model proposed in [28] and the results are matched with the analytical derivation for vertical-orientated UEs as well. It is shown that the lower bound of FOV for TPR and PR are 20° and 30°, respectively.

(2) MRC vs. SBC: The MRC scheme is known to achieve better performance than the SBC scheme when there is no interference in the system. However, this may not be true when the interference is taken into consideration. To demonstrate the performance comparison between the MRC and SBC scheme, the simulation is carried out for different noise levels. In Fig. 11(a), the noise power spectrum density level N_0 is 10^{-20} A²/Hz. When $N_{\rm PD}=3$, the level of interference is slightly higher than the noise, and the MRC schemes achieves similar average SINR as the SBC scheme. With the increase of $N_{\rm PD}$, the noise level becomes higher than the interference level and the system gradually becomes noise dominated. It can be seen that in a noise-limited system, MRC outperforms SBC in terms of average SINR. The noise power spectrum density level N_0 is 10^{-21} A²/Hz in Fig. 11(b). When $N_{\rm PD} \leq 6$, the interference level is higher than the noise level and SBC performs slightly better than MRC. However, the noise starts to rise above the interference level with the further increase of $N_{\rm PD}$ and thus MRC outperforms SBC. For a noise power spectrum density level of 10^{-22} A²/Hz, Fig. 11(c) depicts an interference-limited system and the SBC scheme achieves a higher average SINR than the MRC scheme for all values of $N_{\rm PD}$. In brief, when the system is interference dominated, SBC is a better combining scheme. Otherwise, MRC outperforms SBC when considering the average SINR.

(3) PR vs. TPR: Fig. 12 manifests how the number of PDs $N_{\rm PD}$ affects the system performance for both PR and TPR configurations. The average SINR in Figs. 12(a) and 12(b) exhibit the same tendency. For fair comparisons, it is assumed that the total physical area, $A_t = N_{PD}A_p$, of the ADRs should be the same. Hence, the increase in $N_{\rm PD}$ will lead to the decrease in the physical area A_p on each PD, which means less received power. Nevertheless, when $N_{\rm PD}$ increases from 3 to 6, the average SINR for the PR and TPR both increase. The increase is caused by the decrease in $\Psi_{\rm c,min}$ as displayed in Fig. 10, which leads to a higher channel gain and compensates for the power loss due to the decrease in $A_{\rm p}$. In terms of the PR, the further growth of $N_{\rm PD}$ leads to the decline in the average SINR since $\Psi_{\rm c,min}$ does not change any more. In comparison, the average SINR for the TPR increases until $N_{\rm PD}=9$ as $\Psi_{\rm c.min}$ is still decreasing. When $N_{\rm PD}$ increases from 9 to 10 for the TPR, $\Psi_{\rm c.min}$ decreases slightly from 21° to 20° as demonstrated in Fig. 10. However, the power loss caused by the reduction in A_p exceeds the increase of received power gained from the small decrease in $\Psi_{\rm c,min}$, and thus the average SINR drops. Considering $N_{\rm PD} \geq$ 10, $\varPsi_{\rm c,min}$ is fixed and the average SINR declines as A_p reduces. Hence, in terms of the average SINR, the optimum values of $N_{\rm PD}$ are 6 and 9 for PR and TPR, respectively. It can also be observed that the PR outperforms the TPR with regard to both the average SINR and average data rate when $N_{\rm PD} \leq 6$ since the PR has smaller $\Psi_{\rm c,min}$. On the other hand, when

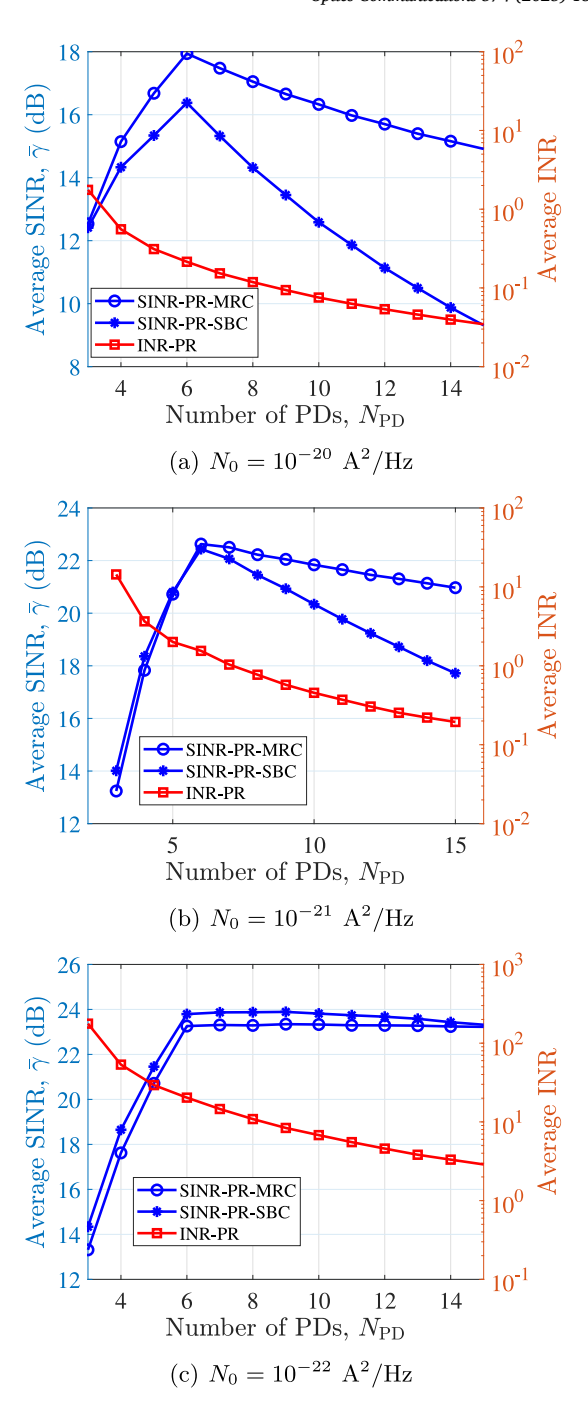


Fig. 11. The performance comparison between MRC and SBC for the SS (PR, B_t =100 MHz).

 $N_{\rm PD} >$ 6, the TPR has smaller $\Psi_{\rm c,min}$ than the PR and hence achieves better performance.

(4) Receiver bandwidth vs. transmitter bandwidth: Based on (22), the relationship between the receiver bandwidth, $B_{\rm r}$, and the number of PDs, $N_{\rm PD}$, is manifested in Fig. 13. When $N_{\rm PD}$ increases from 3 to 15, the bandwidth increases from 150 MHz to around 350 MHz due to the decrease in the physical area of each PD. The communication bandwidth $B_{\rm L}$ is the minimum value between the receiver bandwidth and the transmitter bandwidth, which is denoted as $B_{\rm L} = \min(B_{\rm r}, B_{\rm t})$. The user data rate is determined by the SINR and the communication bandwidth. When the transmitter bandwidth $B_{\rm t}$ is 100 MHz, which is less than $B_{\rm r}$ for all values of $N_{\rm PD}$ in Fig. 13, the communication

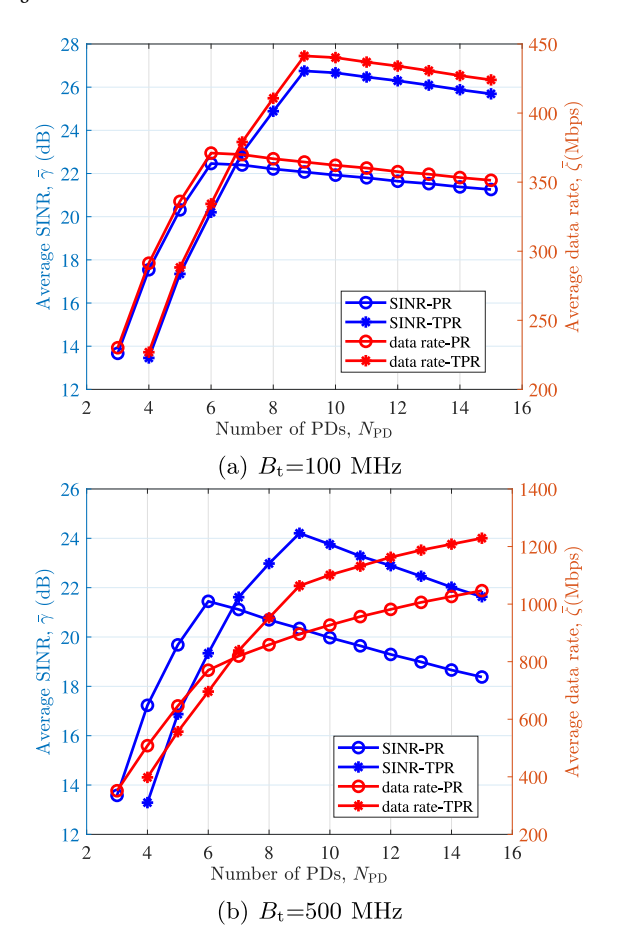


Fig. 12. The performance comparison between PR and TPR configurations considering different transmitter bandwidth in the SS system (MRC, $N_0=10^{-21}~{\rm A^2/Hz}$).

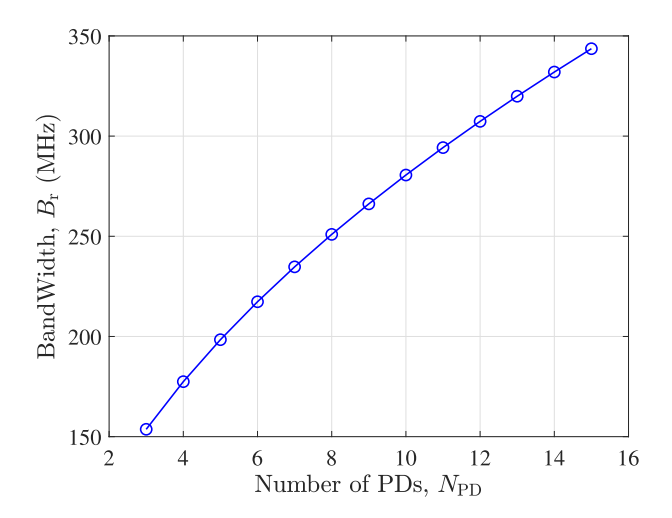


Fig. 13. Receiver bandwidth versus the number of PDs, N_{PD} .

bandwidth is limited by the transmitter and thus $B_{\rm L}=100$ MHz. As $B_{\rm L}$ does not vary according to $N_{\rm PD}$, the average data rate follows the same trend as the average SINR in Fig. 12(a). By increasing the transmitter bandwidth $B_{\rm t}$ to 500 MHz, $B_{\rm r} \leq B_{\rm t}$ for all $N_{\rm PD}$ and the communication bandwidth is limited by the receiver side. Hence, the communication bandwidth $B_{\rm L}=B_{\rm r}$. In Fig. 12(b), with the increase of $N_{\rm PD}$, the average SINR first increases and then decreases, which peaks at $N_{\rm PD}=6$ and $N_{\rm PD}=9$ for the PR and TPR, respectively. In contrast, when $N_{\rm PD}$ grows,

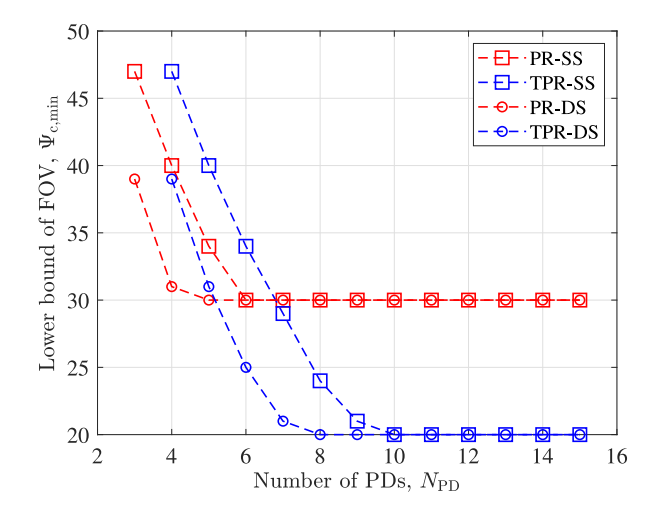


Fig. 14. The relationship between $\Psi_{\rm c,min}$ and the number of PDs, $N_{\rm PD}$, on an ADR for the DS system.

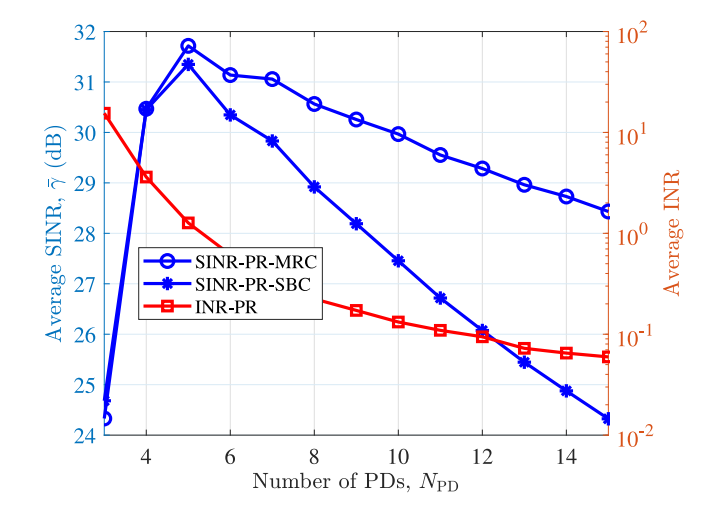


Fig. 15. The performance comparison between MRC and SBC in DS cells (PR, $N_0=10^{-22}$ A²/Hz, B_i =100 MHz).

the average data rate increases even when the SINR degrades, which is due to the greater bandwidth. To sum up, the PR with $N_{\rm PD}=6$ and TPR with $N_{\rm PD}=9$ achieve the highest average data rate for transmitter-bandwidth-limited systems whereas the average data rate peaks at $N_{\rm PD}=15$ in a receiver-bandwidth-limited system for both PR and TPR.

6.4. Performance analysis for DS cells

- (1) Lower bound of FOV: Fig. 14 demonstrates the change in the minimum FOV against the number of PDs for the DS configuration. As shown for the PR, with the increase in $N_{\rm PD}$, the lower bound of FOV $\Psi_{\rm c,min}$ for the DS cells decreases and converges to 30° at $N_{\rm PD}=5$, which is earlier than the SS configuration. When $N_{\rm PD}\leq 5$, the $\Psi_{\rm c,min}$ for the DS configuration is lower than the counterpart in the SS configuration. In terms of the TPR, the minimum FOV for DS converges to 20° at $N_{\rm PD}=8$ and has smaller $\Psi_{\rm c,min}$ than the SS when $N_{\rm PD}\leq 9$.
- (2) MRC vs. SBC: Previously, in Fig. 11(c), we have shown the performance comparison between the MRC and SBC for the SS system with $N_0=10^{-22}~{\rm A^2/Hz}$. Due to the low level of noise power spectral density, the system is mostly interference-limited and SBC outperforms MRC for all given values of $N_{\rm PD}$. By adopting the DS configuration, as shown in Fig. 15, the average interference to noise ratio (INR) is

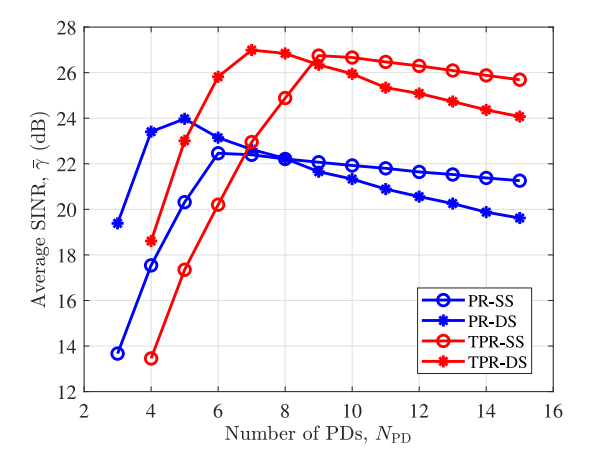


Fig. 16. The performance comparison between PRs and TPRs in DS cells (MRC, $N_0=10^{-21}~{\rm A^2/Hz}$).

larger than 1 only when there are 3 or 4 PDs on the PR. Whereas for $N_{\rm PD} \geq 5$, the noise plays a similar or more important role than the interference. Therefore, compared with the SS system, for the same level of noise power spectral density, the average INR of the DS system degrades substantially. This indicates that the DS system can mitigate interference. With regards to the average SINR, MRC and SBC have similar performance when $N_{\rm PD} \leq 4$ whereas MRC outperforms SBC for $N_{\rm PD} > 4$. From the above analyses, it can be deducted that MRC is a better combining scheme for the DS system with respect to the three different levels of N_0 given previously in this study.

(3) PR vs. TPR: Fig. 16 illustrates the performance comparison between PR and TPR configurations. With respect to the PR, when $N_{\rm PD}$ rises from 3 to 5, the average SINR increases from 19.3 dB to 24 dB, where the increment comes from the decline in $\Psi_{\rm c,min}$. For the same reason, with regards to the TPR, the average SINR grows from 18.5 dB to 27 dB when $N_{\rm PD}$ increases from 4 to 7. The PR and TPR achieves the peak at $N_{\rm PD} = 5$ and $N_{\rm PD} = 7$ respectively. For both PR and TPR configurations, after the peak points, the average SINR drops due to the reduction in the area A_p of each PD, which leads to less physical power. With regard to TPR, changing $N_{\rm PD}$ from 7 to 8 results in the decrease in $\Psi_{\rm c.min}$, which leads to a channel gain boost. However, the gain cannot compensate for the power loss stems that from the reduction in $A_{\rm p}$ and thus the system performance degrades. When $N_{\rm PD} \leq 5$, the PR outperforms the TPR, otherwise, the TPR is a preferred structure. In conclusion, the optimum number of PDs is 5 and 7 for PRs and TPRs, respectively. In addition, the TPR with $N_{\rm PD}=7$ outperforms the PR with $N_{\rm PD}=5$ in terms of the average SINR.

(4) DS vs. SS: Fig. 17 demonstrates the performance comparison between the DS system and the SS system with respect to different levels of noise power spectrum density, N_0 . The typical value of N_0 for a PD is 10^{-21} A²/Hz, at which the DS system achieves a slightly higher average SINR than the SS system for both PRs and TPRs. By reducing the noise power spectrum density level to 10^{-22} A²/Hz, the system becomes interference-limited. With the aid of the DS configuration, the ADR can suppress the signal power from interfering APs by attenuating the NLOS path. Hence, when $N_0 = 10^{-22} \text{ A}^2/\text{Hz}$, the average SINR of DS cells is 7 dB and 5 dB higher than the average SINR of SS cells for PRs and TPRs, respectively. For a noise spectrum density level of 10^{-20} A²/Hz, the system becomes noise limited, in which the DS could not improve system performance by reducing the power of interference signal. In addition, the received power is halved when the DS configuration is applied, and thus the SS outperforms the DS in terms of the average SINR.

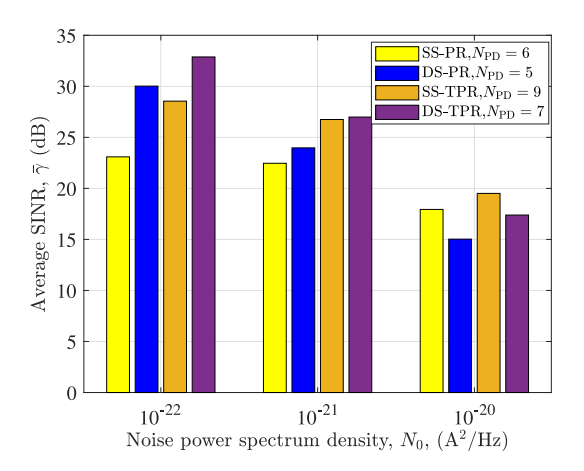


Fig. 17. The performance comparison between the DS and SS systems.

7. Conclusions

This paper investigates the ICI mitigation in LiFi networks using ADRs. The impact of the diffuse link considering random UE orientation is studied and it is shown that both LOS and diffuse links have an important influence on the system performance. The performance of different ADR structures are compared and the optimised ADR structure is proposed for the considered scenario, where the method can be extended to other scenarios easily. By studying systems with different levels of noise power spectrum density, we showed that when the system is noise-limited, MRC outperforms SBC, otherwise, SBC is the preferred combining scheme. In an interference-limited system or noise-plus-interference limited system, the adoption of the DS cell configuration can further mitigate the NLOS interference and thus improve the system performance. However, the limitation of the DS cell is that the transmit power is equally split to the positive and negative sources, which degrades the performance of the noise-limited system.

CRediT authorship contribution statement

Zhihong Zeng: Writing – review & editing, Writing – original draft, Visualization, Validation, Supervision, Software, Resources, Project administration, Methodology, Investigation, Funding acquisition, Formal analysis, Data curation, Conceptualization. Chen Chen: Writing – review & editing, Project administration, Investigation, Funding acquisition. Xiping Wu: Conceptualization, Funding acquisition, Supervision, Validation, Writing – review & editing. Svetislav Savović: Supervision, Investigation. Mohammad Dehghani Soltani: Formal analysis, Conceptualization. Majid Safari: Supervision. Harald Haas: Supervision, Methodology, Conceptualization.

Declaration of competing interest

The authors declare the following financial interests/personal relationships which may be considered as potential competing interests: Chenchen reports financial support was provided by National Natural Science Foundation of China. Xiping Wu reports financial support was provided by National Natural Science Foundation of China. If there are other authors, they declare that they have no known competing financial interests or personal relationships that could have appeared to influence the work reported in this paper.

Data availability

No data was used for the research described in the article.

Appendix A. Proof of (27)

The visible area of the 1-st PD with $\omega_{\rm PD}^1=0$ is illustrated in Fig. 7a. The point **O** represents the location of the UE, $\mathbf{p}_{\rm UE}$, and **OE** represents the normal vector of the PD. The intersection point of the normal vector with the ceiling is **E**. The coordinate of **E** is denoted as $(x_{\rm e}, y_{\rm e}, z_{\rm e})$ and points **A**, **B**, **C**, **D**, **F** are denoted in the same way. Points **A** and **B** are the vertices of the ellipse. Points **C** and **D** are the co-vertices of the ellipse. The centre point of the ellipse is denoted as **F**. The angle between each of the four vectors, **OA**, **OB**, **OC**, **OD** with **OE** is $\Psi_{\rm c}$. The length of the semi-major and semi-minor axes of the ellipse are represented by a and b separately. The length of semi-major axes a is denoted as:

$$a = \frac{|\mathbf{A}\mathbf{B}|}{2} = \frac{h\sin(2\Psi_{c})}{\cos(2\Psi_{c}) + \cos(2\Theta_{PD})}.$$
 (47)

As **A**, **B**, **E**, **F** and **O** are on the same xz-plane, $y_a = y_b = y_e = y_f = y_{\rm UE}$. As **A**, **B**, **C**, **D**, **E** and **F** are on the ceiling, $z_a = z_b = z_c = z_d = z_f = z_e = z_{\rm AP}$, where $z_{\rm AP}$ is the height of the AP. As **C** and **D** are on the same yz-plane with **F**, the coordinates x of these points are represented by:

$$\begin{aligned} x_{\rm c} &= x_{\rm d} = x_{\rm f} = x_{\rm UE} + (a - h \tan(\Psi_{\rm c} - \Theta_{\rm PD})) \\ &= x_{\rm UE} + \frac{h \sin(2\Theta_{\rm PD})}{\cos(2\Psi_{\rm c}) + \cos(2\Theta_{\rm PD})}. \end{aligned} \tag{48}$$

From Fig. 7, we know that $x_{\rm e}=h\tan(\Theta_{\rm PD})+x_{\rm UE}$. Based on the parameters above, we have ${\bf OE}=(h\tan(\theta_{\rm PD}),0,h)$ and ${\bf OC}=(\frac{h\sin(2\Theta_{\rm PD})}{\cos(2\Psi_{\rm c})+\cos(2\Theta_{\rm PD})},b,h)$. Since $\cos(\Psi_{\rm c})=\frac{{\bf OE}\cdot{\bf OC}}{|{\bf OE}||{\bf OC}|},$ b can be obtained as:

$$b = \frac{\sqrt{2}h\sin(\Psi_{\rm c})}{\sqrt{\cos(2\Psi_{\rm c}) + \cos(2\Theta_{\rm PD})}}.$$
 (49)

Consequently, the equation of the ellipse is thus given by:

$$\frac{(x_{\text{ellipse}} - x_{\text{f}})^2}{a^2} + \frac{(y_{\text{ellipse}} - y_{\text{f}})^2}{b^2} = 1.$$
 (50)

The visible area of pth PD can be obtained by rotating the visible area of the 1-st PD around the line ($x = x_{\text{UE}}, y = y_{\text{UE}}$) with an angle of $\omega_{\text{PD},p}$.

Appendix B. Proof of (39)

Substituting (37) and (38) into (36), we can get:

$$-d_{\rm c}\cos\omega_{\rm c}\tan(\Theta_{\rm PD}) = h - \frac{\sqrt{h^2 + d_{\rm c}^2\cos(\Psi_{\rm c})}}{\cos(\Theta_{\rm PD})}. \tag{51}$$

Substituting (32) into (51), the elevation angle of each PD, $\Theta_{\rm PD}$, on PRs is derived as:

$$\Theta_{\rm PD} = F_1(d_{\rm c}) = \tan^{-1} \frac{f_1(d_{\rm c})}{f_2(d_{\rm c})},$$
 (52)

where

$$\begin{split} f_1(d_{\rm c}) &= \sqrt{h^2 + d_{\rm c}^2} \cos(\Psi_{\rm total}) - h, \\ f_2(d_{\rm c}) &= d_{\rm c} \cos(\omega_{\rm c}) - \sqrt{h^2 + d_{\rm c}^2} \sin(\Psi_{\rm total}). \end{split} \tag{53}$$

The function F_1 has one zero at $z_1 = h \tan(\Psi_{\text{total}})$ and one pole at $p_1 = \frac{h \sin(\Psi_{\text{total}}) - (\omega_c)}{\sqrt{\cos^2(\Psi_{\text{total}}) - \sin^2(\omega_c)}}$. The derivative of $F_1(d_c)$ is given by:

$$\frac{\partial F_1}{\partial d_{\rm c}} = -\frac{h^2\cos(\omega_{\rm c})\cos(\varPsi_{\rm total}) - h\sqrt{h^2 + d_{\rm c}^2}\cos(\omega_{\rm c}) + hd_{\rm c}\sin(\varPsi_{\rm total})}{(f_1^2(d_{\rm c}) + f_2^2(d_{\rm c}))\sqrt{h^2 + d_{\rm c}^2}}. \tag{54}$$

By calculating the d_c satisfying $\frac{\partial F_1}{\partial d_c} = 0$, the two roots are denoted as:

$$d_{c1} = \frac{h\cos(\omega_{c})\sin(\Psi_{total})}{\cos(\Psi_{total}) - \sin(\omega_{c})}, \quad d_{c2} = \frac{h\cos(\omega_{c})\sin(\Psi_{total})}{\cos(\Psi_{total}) + \sin(\omega_{c})}.$$
 (55)

When $\sin(\omega_{\rm c}) < \cos(\Psi_{\rm total})$, it can be proven that $0 < d_{\rm c2} < z_1 = h \tan(\Psi_{\rm total}) < d_{\rm c1}$ and $z_1 \le p_1$. In addition, $\frac{\partial^2 F_1(d_{\rm c2})}{\partial^2 d_{\rm c}} < 0$.

Therefore, for $d_c \in (0, h \tan(\Psi_{\text{total}})]$, F_1 has a local maximum at d_{c2} . When $\sin(\omega_c) \geq \cos(\Psi_{\text{total}})$, p_1 and d_{c1} do not have real value. It can also be proved that $0 < d_{c2} < z_1$ and $\frac{\partial^2 F_1(d_{c2})}{\partial^2 d_c} < 0$. Similarly, for $d_c \in (0, h \tan(\Psi_{\text{total}})]$, there is a local maximum at d_{c2} . In summary, the upper bound of F_1 is thus given by:

$$F_{1,\text{max}} = \begin{cases} F_{1}(d_{c2}), & \text{if } d_{c,\text{min}} \le d_{c2} \\ F_{1}(d_{c,\text{min}}), & \text{otherwise.} \end{cases}$$
 (56)

According to (32), Ψ_c is given by:

$$\Psi_{\rm c} = F_2(d_{\rm c}) = \Psi_{\rm total} - F_1(d_{\rm c}).$$
 (57)

Hence, the lower bound of F_2 is denoted as:

$$F_{2,\min} = \begin{cases} F_2(d_{c2}), & \text{if } d_{c,\min} \le d_{c2} \\ F_2(d_{c,\min}), & \text{otherwise.} \end{cases}$$
 (58)

References

- [1] H. Haas, L. Yin, Y. Wang, C. Chen, What is LiFi? J. Lightwave Technol. 34 (6) (2016) 1533–1544.
- [2] T. Borogovac, M. Rahaim, J.B. Carruthers, Spotlighting for visible light communications and illumination, in: 2010 IEEE Globecom Workshops, 2010, pp. 1077–1081.
- [3] K. Cui, J. Quan, Z. Xu, Performance of indoor optical femtocell by visible light communication, Opt. Commun. 298–299 (2013) 59–66.
- [4] C. Chen, S. Videv, D. Tsonev, H. Haas, Fractional frequency reuse in DCO- OFDM-based optical attocell networks, Lightwave Technol J. 33 (19) (2015) 3986–4000.
- [5] C. Chen, D. Tsonev, H. Haas, Joint transmission in indoor visible light communication downlink cellular networks, in: 2013 IEEE Globecom Workshops, (GC Wkshps), 2013, pp. 1127–1132.
- [6] Z. Chen, D.A. Basnayaka, H. Haas, Space division multiple access for optical attocell network using angle diversity transmitters, J. Lightwave Technol. 35 (11) (2017) 2118–2131.
- [7] G.W. Marsh, J.M. Kahn, Channel reuse strategies for indoor infrared wireless communications, communications, IEEE Trans. 45 (10) (1997) 1280–1290.
- [8] J.M. Kahn, J.R. Barry, Wireless infrared communications, Proc. IEEE 85 (2) (1997) 265–298.
- [9] Z. Chen, D. Basnayaka, X. Wu, H. Haas, Interference mitigation for indoor optical attocell networks using angle diversity receiver, J. Lightwave Technol. 2018, 1.
- [10] Z. Zeng, M.D. Soltani, M. Safari, H. Haas, Angle diversity receiver in LiFi cellular networks, in: ICC 2019-2019 IEEE International Conference on Communications, (ICC), 2019, pp. 1–6.
- [11] Z. Zeng, M.D. Soltani, X. Wu, H. Haas, Access point selection scheme for LiFi cellular networks using angle diversity receivers, in: 2019 IEEE Wireless Communications and Networking Conference, (WCNC), 2019, pp. 1–6.
- [12] H.B. Eldeeb, H.A. Selmy, H.M. Elsayed, R.I. Badr, Co-channel interference cancellation using constraint field of view ADR in VLC vhannel, in: 2017 IEEE Photonics Conference (IPC) Part II. IEEE, 2017, Conference Proceedings.
- [13] H.B. Eldeeb, H.A.I. Selmy, H.M. Elsayed, R.I. Badr, Interference mitigation and capacity enhancement using constraint field of view ADR in downlink VLC channel, IET Commun. 12 (16) (2018) 1968–1978.
- [14] M.K. Aljohani, O.Z. Aletri, K.D. Alazwary, M.O.I. Musa, T.E.H. El-Gorashi, M.T. Alresheedi, J.M.H. Elmirghani, NOMA visible light communication system with angle diversity receivers, in: 2020 22nd International Conference on Transparent Optical Networks, (ICTON), IEEE, 2020, Conference Proceedings.
- [15] H.B. Eldeeb, H.A.I. Selmy, H.M. Elsayed, R.I. Badr, M. Uysal, Efficient resource allocation scheme for multi-user hybrid VLC/IR networks, in: 2019 IEEE Photonics Conference, (IPC), IEEE, 2019, Conference Proceedings.
- [16] H.B. Eldeeb, M. Hosney, H.M. Elsayed, R.I. Badr, M. Uysal, H.A.I. Selmy, Optimal resource allocation and interference management for multi-user uplink light communication systems with angular diversity technology, IEEE Access 8 (2020) 203 224–203 236.
- [17] S. Chi, P. Wang, S. Niu, H. Che, Z. Wang, Y. Wu, Uniformity improvement on received optical power for an indoor visible light communication system with an angle diversity receiver, Appl. Opt. 60 (26) (2021) 8031–8037, [Online]. Available: https://www.ncbi.nlm.nih.gov/pubmed/34613064.
- [18] M. Román Cañizares, P. Palacios Játiva, C.A. Azurdia-Meza, S. Montejo-Sánchez, S. Céspedes, Impact of diversity combining schemes in a multi-cell VLC system with angle diversity receivers, in: Photonic Network Communications, vol. 43, (1) pp. 13–22, 202.
- [19] R. Harada, C.T. Geldard, W.O. Popoola, Performance analysis of angular diversity receivers in multi-cell VLC systems, in: GLOBECOM 2023-2023 IEEE Global Communications Conference, IEEE, 2023, Conference Proceedings.
- [20] A.G.A. Al-Sakkaf, M. Morales-Céspedes, Interference management for VLC indoor systems based on overlapping field-of-view angle diversity receivers, in: IEEE Access, vol. 12, 2024, pp. 51 431–51 449.

- [21] D. Sabui, S. Chatterjee, A. Prakash, B. Roy, G.S. Khan, Design of an off-axis freeform diversity receiver to improve SINR performance of a multi-cell VLC system, Opt. Commun. 510 (2022).
- [22] S. Chatterjee, D. Sabui, B. Roy, Mobility aware blockage management of a multiuser multi-cell hybrid Li-Fi Wi-Fi system with freeform diversity receiver, Opt. Commun. 560 (2024).
- [23] M.L.N. Kumar, D. Sen, P. Mohapatra, Performance evaluation of MIMO modulation schemes for indoor VLC channels with angular detectors, in: 2019 IEEE 90th Vehicular Technology Conference, (VTC2019-Fall), IEEE, 2019, Conference Proceedings.
- [24] V. Dixit, A. Kumar, Performance analysis of angular diversity receiver based MIMO-VLC system for imperfect CSI, J. Opt. 23 (8) (2021) 085701.
- [25] A. Nuwanpriya, S.W. Ho, C.S. Chen, Indoor MIMO visible light communications: Novel angle diversity receivers for mobile users, IEEE J. Sel. Areas Commun. 33 (9) (2015) 1780–1792.
- [26] C. Chen, W.D. Zhong, H. Yang, S. Zhang, P. Du, Reduction of SINR fluctuation in indoor multi-cell VLC systems using optimized angle diversity receiver, J. Lightwave Technol. (2018) 1.
- [27] V. Dixit, A. Kumar, Error performance of an L-PPM modulated ADR-based MIMO-VLC system with and without channel estimation error, Appl. Opt. 62 (10) (2023) 2501–2509, dixit, Vipul Kumar, Atul eng 2023/05/03 Appl Opt. 2023 Apr 1;62(10):2501-2509. DOI: 10.1364/AO.478994. [Online]. Available: https://www.ncbi.nlm.nih.gov/pubmed/37132798, https://opg.optica.org/ao/abstract.cfm?uri=ao-62-10-2501.

- [28] M.D. Soltani, A.A. Purwita, Z. Zeng, H. Haas, M. Safari, Modeling the random orientation of mobile devices: Measurement, analysis and LiFi use case, IEEE Trans. Commun. 67 (3) (2019) 2157–2172.
- [29] Z. Zeng, M.D. Soltani, H. Haas, M. Safari, Orientation model of mobile device for indoor VLC and millimetre wave systems, in: Accepted in 2018 IEEE 88nd Vehicular Technology Conference, (VTC2018-Fall), Chicago, USA, 2018.
- [30] M.S. Alouini, A.J. Goldsmith, Area spectral efficiency of cellular mobile radio systems, vehicular technology, IEEE Trans. 48 (4) (1999) 1047–1066.
- [31] C. Chen, D.A. Basnayaka, H. Haas, Downlink performance of optical attocell networks, J. Lightwave Technol. 34 (1) (2016) 137–156.
- [32] H. Schulze, Frequency-domain simulation of the indoor wireless optical communication channel, IEEE Trans. Commun. 64 (6) (2016) 2551–2562.
- [33] S. Dimitrov, H. Haas, Optimum signal shaping in OFDM-based optical wireless communication systems, in: Vehicular Technology Conference (VTC Fall), 2012, IEEE, 2012, pp. 1–5.
- [34] S.M. LaValle, Planning. Algorithms, Planning Algorithms Cambridge, Cambridge University Press, Cambridge, 2006.
- [35] S.B. Alexander, Optical Communication Receiver Design, (37) IET, 1997.
- [36] Z. Chen, D. Tsonev, H. Haas, A novel double-source cell configuration for indoor optical attocell networks, in: 2014 IEEE Global Communications Conference, 2014, pp. 2125–2130.